Sentinel-2 remote sensing of Zostera noltei-dominated intertidal seagrass meadows

Maria Laura Zoffoli, Pierre Gernez, Philippe Rosa, Anthony Le Bris, Vittorio E. Brando, Anne-Laure Barillé, Nicolas Harin, Steef Peters, Kathrin Poser, Lazaros Spaias, et al.

Sentinel-2 remote sensing of *Zostera noltei*-dominated intertidal seagrass meadows

Maria Laura Zoffoli[1*], Pierre Gernez[1], Philippe Rosa[1], Anthony Le Bris[1,2], Vittorio E. Brando[3], Anne-Laure Barillé[4], Nicolas Harin[4], Steef Peters[5], Kathrin Poser[5,6], Lazaros Spaias[5], Gloria Peralta[7] and Laurent Barillé[1]

[1]Université de Nantes, Laboratoire Mer Molécules Santé, Faculté des Sciences, 2 rue de la Houssinière, 44322, Nantes, France

[2]Currently at Ecology and Environment department (EENVI), Algae Technology and Innovation Centre (CEVA), 22610, Pleubian, France

[3]Institute of Marine Sciences, National Research Council of Italy (CNR-ISMAR), 00133, Rome, Italy

[4]Bio-littoral, Faculté des Sciences et des Techniques, B.P. 92 208, 44322, Nantes, France

[5]Water Insight, 6709 PG 22, Wageningen, The Netherlands

[6]Currently at German Aerospace Center (DLR), Cologne, Germany

[7]Department of Biology, Faculty of Environmental and Marine Sciences, University of Cadiz, 11510 Puerto Real, Cadiz, Spain

*Corresponding author: laura.zoffoli@univ-nantes.fr

Highlights

- A method is proposed to map seagrass cover in exposed intertidal meadows.
- The method can be applied to seagrass meadows along the northwest Atlantic coast.
- Sentinel-2-derived seagrass percent cover was mapped with an uncertainty of 14%.
- Due to Sentinel-2 revisit time, it was possible to describe the seasonal cycle.

Abstract

Accurate habitat mapping methods are urgently required for the monitoring, conservation, and management of blue carbon ecosystems and their associated services. This study focuses on exposed intertidal seagrass meadows, which play a major role in the functioning of nearshore ecosystems. Using Sentinel-2 (S2) data, we demonstrate that satellite remote sensing can be used to map seagrass percent cover (SPC) and leaf biomass (SB), and to characterize its seasonal dynamics. *In situ* radiometric and biological data were acquired from three intertidal meadows of *Zostera noltei* along the European Atlantic coast in the summers of 2018 and 2019. This information allowed algorithms to estimate SPC and SB from a vegetation index to be developed and assessed. Importantly, a single SPC algorithm could consistently be used to study *Z. noltei*-dominated meadows at several sites along the European Atlantic coast. To analyze the seagrass seasonal cycle and to select images corresponding to its maximal development, a two-year S2 dataset was acquired for a French study site in Bourgneuf Bay. The potential of S2 to characterize the *Z. noltei* seasonal cycle was demonstrated for exposed intertidal meadows. The SPC map that best represented seagrass growth annual maximum was validated using *in situ* measurements, resulting in a root mean square difference of 14%. The SPC and SB maps displayed a patchy distribution, influenced by emersion time, mudflat topology, and seagrass growth pattern. The ability of S2 to measure the surface area of different classes of seagrass cover was investigated, and surface metrics based on seagrass areas with SPC $\geq$ 50% and SPC $\geq$ 80% were computed to estimate the interannual variation in the areal extent of the meadow. Due to the high spatial resolution (pixel size of 10 m), frequent revisit time ($\leq$ 5 days), and long-term objective of the S2 mission, S2-derived seagrass time-series are expected to contribute to current coastal ecosystem management, such as the European Water Framework Directive, but to also guide future adaptation plans to

face global change in coastal areas. Finally, recommendations for future intertidal seagrass studies are proposed.

Keywords: *Zostera noltei*; seasonal cycle; Earth Observation; Water Framework Directive; mudflats.

1. Introduction

Blue carbon ecosystems, such as seagrass meadows, have the capacity to sequester large amounts of carbon, surpassing even highly productive terrestrial ecosystems, such as tropical forests (McRoy and McMillan, 1977; Krause-Jensen et al., 2018; Saderne et al., 2019). In economic terms, the seagrass contribution to carbon sequestration has been estimated to be 394 US$/ha/yr (Dewsbury et al., 2016). However, the local economic value of this ecosystem service can vary widely, as it is site-specific (Nordlund et al., 2018). Seagrass meadows also provide several other ecosystem services worldwide, such as sediment stabilization, wave energy reduction, regulation of nutrient cycles and water turbidity, and the supply of habitat, refuge, food, and nursery to a variety of faunal species (Nordlund et al., 2016; Dewsbury et al., 2016). For instance, nurseries provided by seagrass ecosystems are associated with approximately 20% of the main fisheries in the world, and this service has been valued at 1.8 million US$/yr (Unsworth et al., 2018; Dewsbury et al., 2016). The overall economic value of seagrass meadow ecosystems has been estimated to be 34,000 US$/ha/yr. However, many gaps in the seagrass values used in such estimates remain (Costanza et al., 1997; Barbier et al., 2011; Dewsbury et al. 2016). Because of the services they provide, seagrass meadows are considered to be indicators of the health of the coastal ocean (Borum and Sand-jensen, 2019; Duarte, 1995). Seagrass ecosystems are vulnerable to natural and anthropogenic threats, including impacts generated in adjacent marine and terrestrial ecosystems, which are

responsible for the worldwide reduction and fragmentation of these valuable habitats. Such impacts include disease, natural disasters, nearshore urbanization and coastal development, dredging, reduction in water quality, introduction of non-native species, thermal stress, climate change, sediment contamination, and sea level rise (Duffy et al., 2019; Lin et al., 2018; Orth et al., 2006; Phinn et al., 2018a; Soissons et al., 2018; Valle et al., 2014; Waycott et al., 2009, 2005).

In order to establish a reference baseline of seagrass status, and to efficiently monitor, manage, and protect seagrass ecosystems, detailed knowledge of their worldwide spatial distribution and temporal dynamics is needed, in terms of percent cover, biomass, and primary production (Unsworth et al., 2019; Waycott et al., 2005; Hossain et al., 2015). However, mapping seagrass distribution is very challenging due to its widespread and dynamic nature. Large uncertainties therefore remain in global estimates of seagrass cover, with estimates of total area ranging ~7 fold, from 15 to 100 Mha (Short et al., 2007; Pendleton et al., 2012; Nordlund et al., 2018; Sani et al., 2019; Duffy et al., 2019). In particular, many regions predicted to support vast meadows are still uncharted. Obtaining and maintaining up-to-date information on seagrass distribution has been identified as one of the main challenges for seagrass conservation (Unsworth et al., 2019).

Since the 1990s, remote sensing has been proven to be an efficient, synoptic, and cost-effective tool to monitor and map seagrass (Calleja et al., 2017; Ferguson and Korfmacher, 1997; Hossain et al., 2015; Kutser et al., 2020; Lyons et al., 2013; Mumby and Harborne, 1999; Roelfsema et al., 2014; Ward et al., 2003). Since the launch of the Landsat mission, seagrass mapping has benefited from an uninterrupted increase in satellite data quality, computing capability, and integration with *in situ* measurements, which together have boosted the use of remote sensing data for seagrass studies (Dekker et al., 2005). The use of remote sensing techniques is more challenging for seagrass landscapes than for terrestrial ones, due in

100 part to differences in spatial extent, which is usually much smaller for seagrass habitats.
101 Compared to terrestrial areas, the spatial distribution of seagrass meadows is generally
102 restricted to narrow and fragmented areas stretching along the coast. This type of spatial
103 distribution limits the utility of medium resolution satellites (spatial resolution > 250 m) for
104 seagrass mapping, as the seagrass signal can be masked by intra-pixel mixtures with other
105 cover types. However, this is less of an issue for high spatial resolution remote sensing (≤ 10
106 m), which enables small-scale features to be detected (Hedley et al., 2016; Kutser et al.,
107 2020). In this case, the main issue is instead obtaining enough suitable images to estimate
108 seagrass dynamics, as the satellite revisit time may be insufficient, with cloud cover further
109 reducing the number of exploitable images (Hedley et al., 2016; Hestir et al., 2015; Kovacs et
110 al., 2018). Additional limitations are expected for intertidal seagrass remote sensing, given
111 that even a small layer of water overlying the seagrass can introduce noise into the satellite
112 data, and the observation of the meadow can even be impeded below turbid waters. Due to
113 these issues, previous remote sensing studies of intertidal vegetation have been limited to the
114 use of either high spatial/low temporal resolution data, such as Worldview, Pléiades, SPOT,
115 or Landsat missions (Barillé et al., 2010; Echappé et al., 2018; Wang et al., 2018), or to high
116 temporal/coarse spatial resolution data, such as MODIS (van der Wal et al., 2010;
117 Vanhellemont, 2009). However, the launch of the first Sentinel-2 (S2) satellite in 2015 by the
118 European Space Agency (ESA) enables new possibilities. With a constellation of twin
119 satellites (S2A and S2B), the S2 mission now offers an unprecedented combination of high
120 spatial and temporal resolutions at no-cost, suitable for seagrass mapping, as recently
121 demonstrated in shallow water environments (Hedley et al., 2018; Traganos et al., 2018;
122 Traganos and Reinartz, 2018).
123 In comparison with subtidal meadows, intertidal seagrass ecosystems remain understudied
124 (Hossain et al., 2015; Phinn et al., 2018b). Recent remote sensing studies of intertidal seagrass

125 have been based upon classification and machine learning techniques (e.g., Calleja et al.,
126 2017; Duffy et al 2018). Once seagrass areas are identified, quantitative information on cover
127 and biomass distribution is still needed to study spatio-temporal seagrass dynamics and to
128 model their carbon assimilation. In the present study, we explored the potential of S2 to map
129 biological indicators of intertidal seagrass meadows and to characterize their seasonal
130 dynamics. The first objective was therefore to develop and validate algorithms to quantify
131 seagrass cover and biomass of an intertidal meadow dominated by *Zostera noltei* observed
132 during emersion. As the algorithm was principally developed for a North Atlantic case study
133 site, we also investigated the geographic robustness of the percent cover determination for
134 two other intertidal ecosystems located along the European Atlantic coast. The second
135 objective was then to apply the algorithms to S2 imagery to provide high spatial resolution
136 maps of seagrass percent cover and leaf biomass that robustly represent seagrass distribution
137 at its maximal seasonal development. Based on our results, we have provided some practical
138 recommendations for seagrass remote sensing in intertidal areas, toward a consistent and
139 rational framework for further studies on seagrass distribution, dynamics, and trends.
140

141 **2. Materials and Methods**

142 2.1. Study sites

143 *Zostera noltei* generally occupies large extents of the intertidal zone. Its distribution includes
144 the Mediterranean, temperate North Atlantic, and North Pacific ecoregions (Short et al.,
145 2007). Our three study sites were located along the European North Atlantic coast, from 36 to
146 47° N. From north to south, they were: (i) Bourgneuf Bay (France), (ii) Marennes-Oléron Bay
147 (France), and (iii) Cadiz Bay (Spain) (Figure 1a). Bourgneuf Bay was the main study site,
148 with Marennes-Oléron and Cadiz Bays used only for algorithm evaluation.

149 Bourgneuf Bay (2°05′W, 47°00′N) is located along the French Atlantic coast, south of the
150 Loire Estuary (Figure 1e). It is a semi-diurnal macrotidal bay, with a maximal amplitude of 6
151 m. It occupies a surface area of 340 km^2, with one third corresponding to a large intertidal
152 zone (Barillé et al., 2010). In this bay, turbidity is usually so high that benthic vegetation is
153 not visible from above water (Dutertre et al., 2009; Gernez et al., 2014). Large monospecific
154 *Zostera noltei* seagrass beds are located in the southwestern part of the bay (Figure 1b-e),
155 where the coastline is protected from the Atlantic swell by the Noirmoutier Island and a rocky
156 barrier. Beside seagrass, other types of benthic coverage can also be found, although to lesser
157 extents: (i) bare sand and/or mud, (ii) benthic microalgae, and (iii) scattered patches of
158 drifting macroalgae brought by waves and not fixed to the substrate.
159 Marennes-Oléron Bay (1°13′W, 45°56′N) is also located along the French Atlantic coast. It is
160 larger than Bourgneuf Bay, but has similar characteristics in terms of *Z. noltei* dominance and
161 semi-diurnal tidal amplitude. The seagrass meadow, which covers an extensive area
162 approximately 15 km long and 1.5 km wide, is part of a Natura 2000 protected area (Lebreton
163 et al., 2009). As in Bourgneuf Bay, extensive areas of oyster farming activity are located near
164 the seagrass meadow.
165 Cadiz Bay (6°15′W, 36°28′N) is located along the southern Atlantic coast of Spain. The
166 characteristics of the *Z. noltei* meadow in this bay are distinct from those of the French sites,
167 in terms of climate, tidal context, turbidity, and biodiversity. The intertidal area is smaller
168 than the sites along the French Atlantic coast, with a semi-diurnal tidal amplitude of 3.6 m,
169 thus limiting the spatial extent of the seagrass beds. Even when *Z. noltei* dominates the
170 meadow, some patches of *Caulerpa prolifera* and sediment with calcareous algae can be
171 found. Unlike the French sites, the distribution of *Z. noltei* in Cadiz Bay is fragmented.

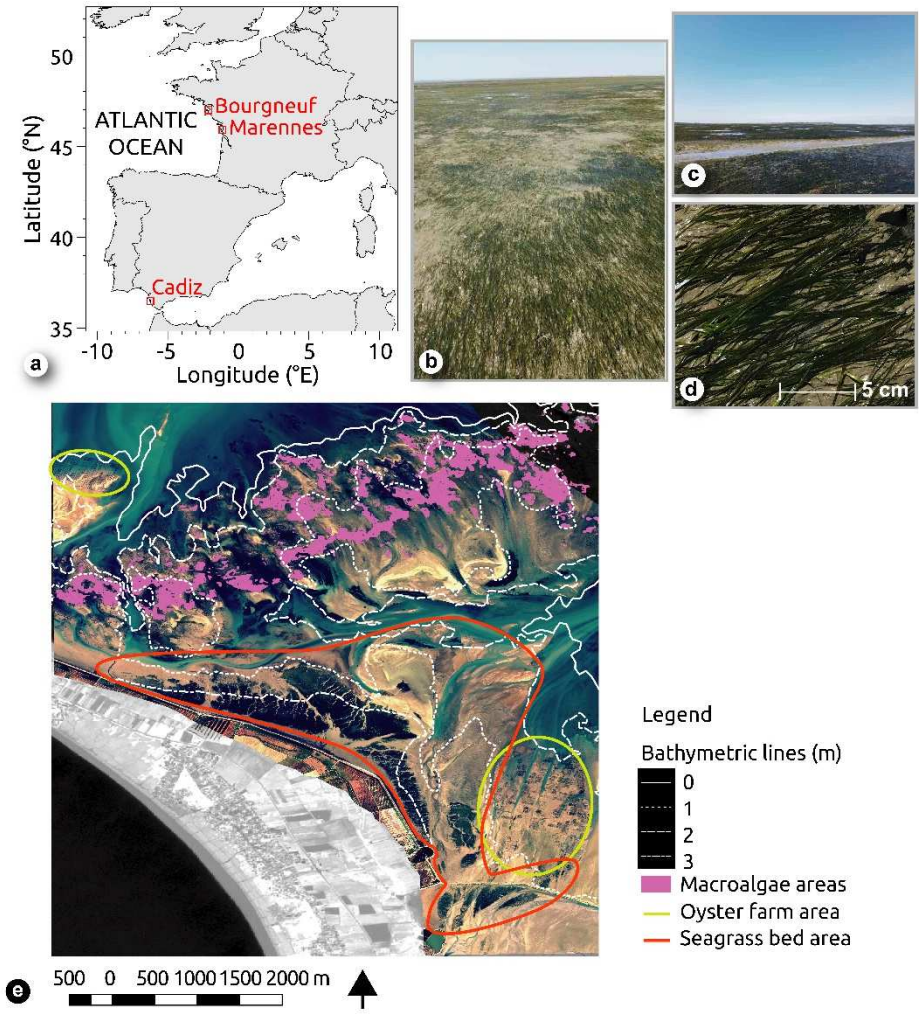

172

173 **Figure 1.**

174

175 2.2. *In situ* measurements

176 Field sampling was always performed during low tide. For each study site, seagrass percent
177 cover (SPC) was determined in conjunction with radiometric measurements for algorithm
178 development and evaluation. In Bourgneuf Bay, seagrass leaf biomass (SB) measurements
179 were additionally performed. Data collection and processing are summarized in Figure 2, and
180 detailed in the following subsections.

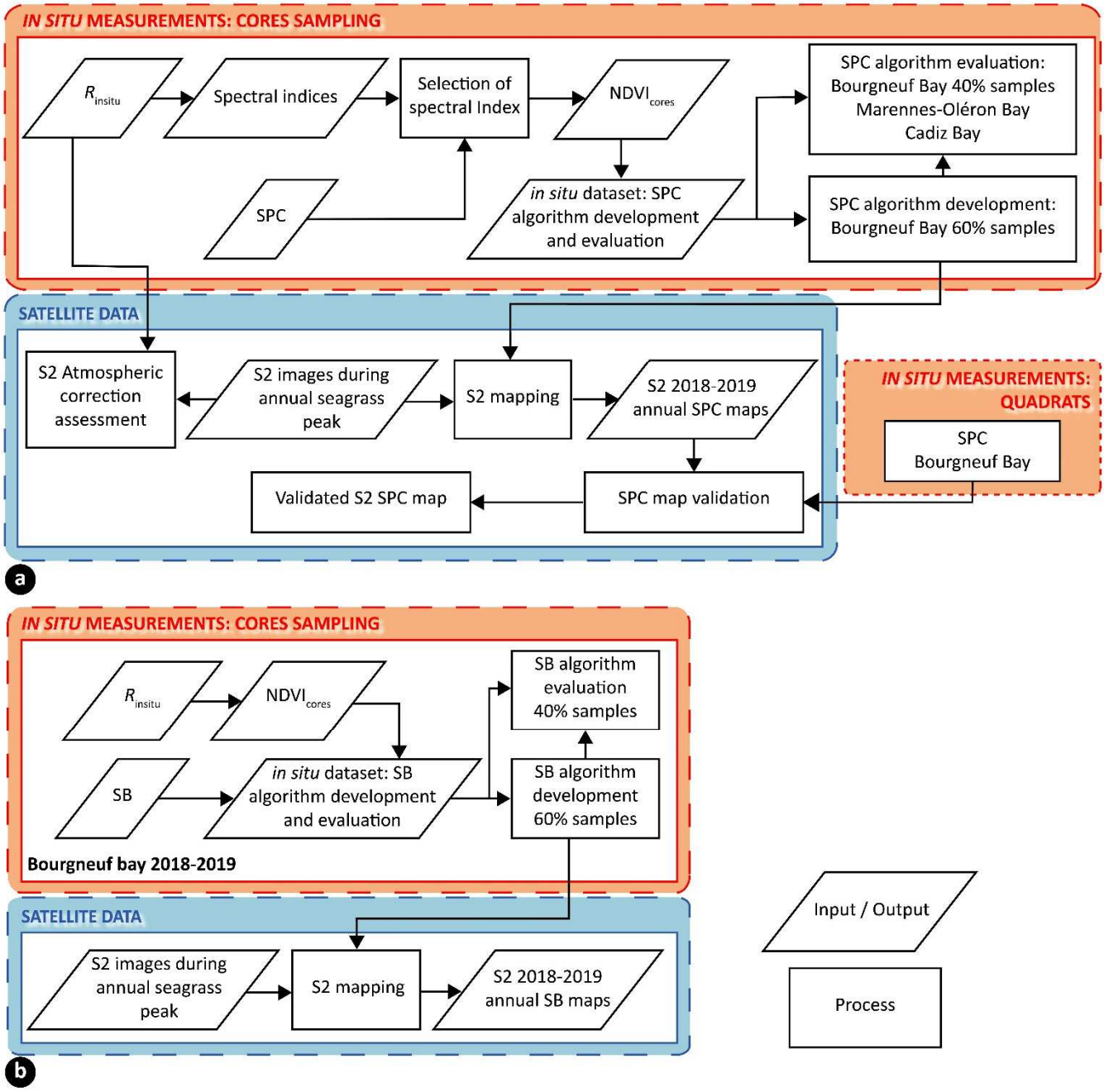

Figure 2.

2.2.1. *In situ* seagrass percent cover and biomass measurements

A total of 131 stations ranging from 0 (bare sediment) to 100% seagrass cover from the three study sites were randomly sampled (Table 1). At each station, SPC over a 20 cm-diameter circle, corresponding to the core area used for biomass sampling (Water Framework Directive -WFD, 2000/60/EC-) (Figure 3a), was measured. For each core surface area, a nadir-viewing

189 photograph of the core surface was acquired, from which seagrass percent cover (SPC_{cores})
190 was computed using the ImageJ software (Diaz-Pulido et al., 2011). To estimate seagrass leaf
191 biomass (SB_{cores}), the sediment below the core area was sampled to a depth of approximately
192 20 cm. Each sample was sieved with a 1 mm mesh and the seagrass leaves were weighted
193 after drying for 48h at 60°C (Bargain et al., 2012; Barillé et al., 2010).
194 Seagrass cover measurements were also performed for satellite retrieval validation along three
195 1 km transects in Bourgneuf Bay, similar to the sampling designs of previous match-up
196 exercises (Phinn et al., 2008; Lyons et al., 2011; Roelfsema et al., 2014). For each transect,
197 sampling stations were separated by at least 40 m to avoid autocorrelation between adjacent
198 stations. The stations corresponded to the center of S2 pixels and were geolocated at
199 submetric accuracy using a Trimble® Geo 7 dGPS. For each pixel, five 0.25 m^2 squares were
200 positioned to form a cross within an area of approximately 25 m^2 so as to take spatial
201 patchiness into account (Burdick and Kendrick, 2001). For each square, SPC was estimated
202 from a nadir-viewing photograph using the ImageJ software. The percent cover of each
203 station was then computed as the average of the five squares (SPC_{insitu}). Unlike percent cover,
204 the biomass map was not validated using *in situ* measurements, because the spatial scale
205 (several 100 m^2 pixels) rendered the destructive *in situ* measurement method unviable.
206
207 **Table 1.**

		Number of samples			
Site (year)	**Dates**	$\boldsymbol{R}_{\mathbf{insitu}}$	$\mathbf{SPC}_{\mathbf{cores}}$	$\mathbf{SB}_{\mathbf{cores}}$	$\mathbf{SPC}_{\mathbf{insitu}}$
Bourgneuf Bay (2018)	Sept. 14, 26, 28	20	20	20	69
Bourgneuf Bay (2019)	Sept. 1, 13, 18	59	59	23	79
Marennes-Oléron (2019)	Sept. 3	28	28	-	-
Cadiz Bay (2019)	Sept. 29	24	24	-	-
Total		131	131	43	148

208

209 2.2.2. *In situ* radiometry

210 The sky was cloud-free during the acquisition of all radiometric data, and all measurements
211 were performed avoiding shadows over the targets. The upwelling radiance (L_{core}, W m^{-2} sr^{-1}
212 nm^{-1}) was measured at nadir from 350 to 2500 nm, at the center of the core surface, using an
213 Analyzed Spectral Device field portable spectroradiometer (ASD Fieldspec). The
214 downwelling radiance ($L_{reference}$, W m^{-2} sr^{-1} nm^{-1}) diffusively reflected by a Spectralon white
215 reference was also measured. The reflectance of the seagrass cover (R_{insitu}, dimensionless) was
216 estimated following Equation 1 (Milton et al., 2007).

217

218 $$R_{\mathrm{insitu}} = \frac{L_{\mathrm{core}}}{L_{\mathrm{reference}}} \quad \text{Eq. 1}$$

219

220 The final dataset consisted of reflectance spectra spanning a range of SPC, from 0 to 100%.
221 As the field work was performed within four-hour periods (corresponding to +/- 2 hours of
222 low tide) and at different latitudes, the sun elevation and viewing geometry varied within the
223 dataset. As a result, the raw reflectance spectra exhibited a large range of variability, due
224 either to differences in seagrass cover and/or in acquisition geometry. In order to minimize the
225 uncertainty caused by differences in measurement conditions, a multiplicative scatter
226 correction (MSC; Isaksson and Kowalski, 1993) previously applied to seagrass reflectance
227 data (Fyfe 2003) was adapted for application to our *in situ* datasets (see appendix for more
228 details). Once corrected, the corresponding reflectance spectra were degraded to the spectral
229 resolution of Sentinel-2A using its spectral response function (SRF; ESA, 2015).

230

231 2.2.3. Selection of the vegetation index

232 Many different vegetation indices (VIs) have previously been applied to multispectral remote
233 sensing images to map intertidal seagrass beds (Bargain et al., 2012). In the present study,

234 several VIs suitable for S2 were tested using the Bourgneuf Bay datasets. An evaluation was
235 performed for each of the following: normalized difference vegetation index (NDVI; Tucker,
236 1979), normalized difference aquatic vegetation index (NDAVI; Villa et al., 2014, 2013),
237 water adjusted vegetation index (WAVI; Villa et al., 2014), soil-adjusted vegetation index
238 (SAVI; Huete, 1988), atmospherically resistant vegetation index (ARVI; Kaufman and Tanré,
239 1992), modified narrow-band NDVI (mNDVI; Bargain et al, 2012), and modified normalized
240 difference (mND; Sims and Gamon, 2002).
241 We evaluated the robustness of each index in terms of differences in the VI *vs.* SPC_{cores}
242 relationship between 2018 and 2019, using an analysis of covariance (ANCOVA) (Table A1).
243 In all cases, a linear regression was obtained. Only those VIs for which significant differences
244 in the slope and intercept between 2018 and 2019 were not found were selected. We then
245 merged the Bourgneuf Bay 2018 and 2019 datasets, and assessed the performance of the
246 linear regression using the coefficient of determination (R^2) and the root mean squared
247 difference (RMSD). The best performance was achieved by the NDVI(665,842),
248 NDVI(705,842), NDAVI(490,842), and ARVI(490,665,842) (Table A1). Besides its good
249 performance, the NDVI(665,842) (hereafter $NDVI_{cores}$) was finally selected for several
250 reasons. First, it has been widely used and could be applied to most historical and current
251 satellite sensors, thus allowing consistent long-term studies. Second, S2 data has a 10 m pixel
252 size at 665 and 842 nm. Seagrass maps computed using other S2 spectral bands could be
253 limited by a larger pixel size (20 or 60 m), thus decreasing the accuracy of the seagrass maps.
254
255 2.2.4. Development and evaluation of seagrass algorithms
256 Algorithm development and evaluation was performed over a large range of $NDVI_{cores}$ (0.12 –
257 0.77), SPC (0 – 100%), and SB (0 – 175.18 g DW m^{-2}) using the Bourgneuf Bay merged
258 dataset (Figure 3). The dataset was randomly split into two groups: one for algorithm

development (60% of data), and one for algorithm evaluation (the remaining 40%). SPC data from the two other sites were also used for algorithm evaluation, and its performance was then evaluated for the three sites independently.

While a linear relationship was found between $NDVI_{cores}$ and SPC_{cores} (Figure 3b), a non-linear relationship was found between $NDVI_{cores}$ and SB_{cores} (Figure 3c). An exponential fit (i.e., $NDVI_{cores} = a \cdot \left(1 - e^{\left(b(SB_{cores}+c)\right)}\right)$) was obtained ($R^2 = 0.92$; $p < 0.001$), but saturation occurred for samples with $NDVI_{cores} \geq 0.65$. We therefore decided to develop the SB algorithm using only samples within the range $0.20 \leq NDVI_{cores} \leq 0.65$, using a linear model.

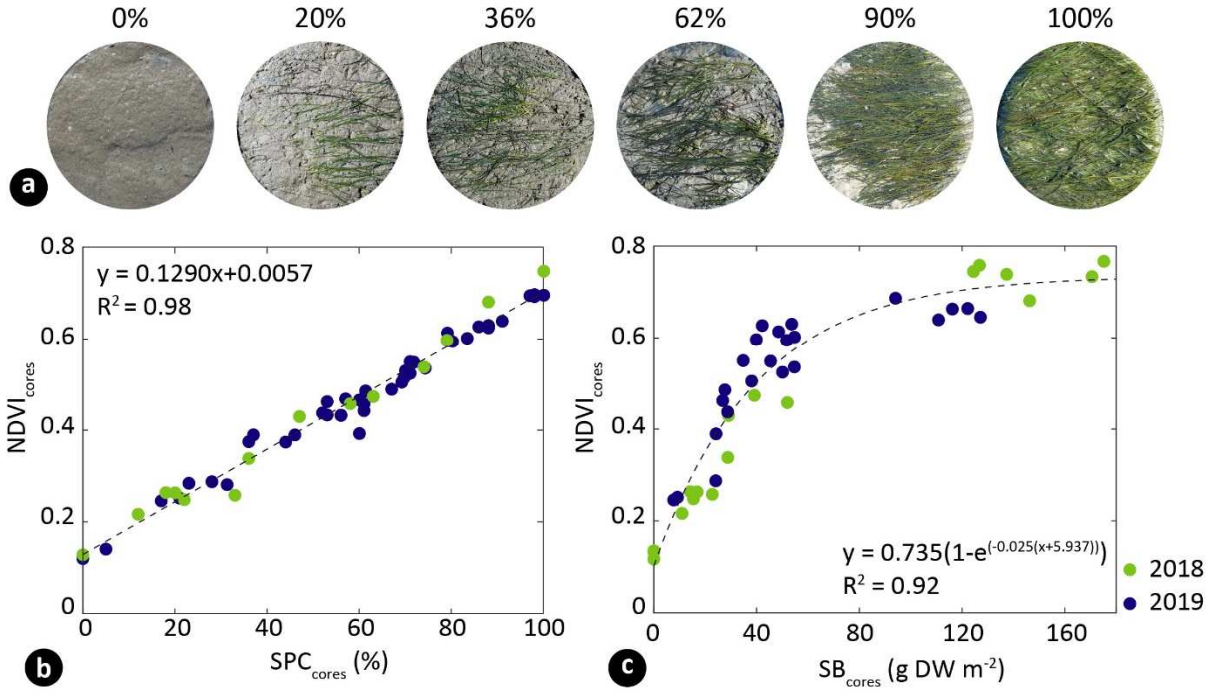

Figure 3.

2.3. Satellite data

2.3.1. S2 image acquisition and processing

Geolocated Level-2A Sentinel-2A/B images of Bourgneuf Bay were downloaded from the European Space Agency (ESA) data portal (https://scihub.copernicus.eu). Level-2A data have

275 already been atmospherically-corrected using the Sen2Cor processor algorithm (Main-Knorn
276 et al., 2017), and were distributed as bottom-of-atmosphere reflectance ($R_{sat\text{-}S2}$,
277 dimensionless). We selected only cloud- and shadow-free low tide images (water level at the
278 harbour of Noirmoutier Island, L'Herbaudière < 3.20 m of the Lowest Astronomical Tide
279 (LAT)), reducing the final S2 dataset to 42 images (see Table A2 for details). All satellite data
280 processing was performed using the Sentinel Application Platform (SNAP; http://step.esa.int).
281 The atmospheric correction performance was evaluated using two S2 scenes and concomitant
282 *in situ* reflectance of three types of targets: bare sediment, full seagrass cover, and mixed
283 substrate. The latter included substrates with bare sediment, seagrass, and/or macroalgae.
284 Different strategies were used for the different target types to obtain the best possible match-
285 ups. For homogeneous areas, namely the areas of bare sediment and dense seagrass cover, the
286 average of the R_{insitu} measurements were compared with the average of several pixels
287 identified as these substrates in the field. For validation over mixed-cover areas, three pixels
288 coinciding with the coordinates of 20 R_{insitu} samples were extracted, and the mean reflectance
289 of those pixels was compared with the mean of the *in situ* measurements.
290 $NDVI_{S2}$ was computed for the entire S2 dataset using the bands centred at 665 and 842 nm.
291 To select only the intertidal zone, we applied a geographical mask based on the bathymetric
292 map provided by the French Naval Hydrographic and Oceanographic Service (SHOM). The
293 lower limit of the selected area was set to 0 m LAT, while the uppermost limit was restricted
294 to 4.5 m LAT (Barillé et al., 2010). Areas of rocky substrate covered by macroalgae near
295 seagrass beds were excluded based on Geographical Information System (GIS) data (Barillé
296 et al., 2010). Finally, pixels outside the 0.12 – 0.80 $NDVI_{S2}$ range were masked. The lower
297 boundary corresponded to either bare sediment (Figure 3b) or contamination by a layer of
298 water. The upper boundary was estimated from our radiometric measurements as the
299 saturation of $NDVI_{cores}$ over dense seagrass cover, plus five percent, which was added to

300 create the upper biomass limit mask to account for very dense biomass that can occur in the
301 field, but which was not included in our dataset. According to Barillé et al. (2010), values
302 higher than 0.8 can be assumed not to correspond to seagrass, but to the accumulation of
303 drifted macroalgae. All SPC and SB maps were reprojected to the WGS84 UTM30N
304 coordinate reference system.
305
306 2.3.2. Assessing seasonal variability for optimal S2 seagrass mapping
307 In order to select the dates most representative of the annual growth peak, the seasonal
308 variability of NDVI was investigated using the 42 selected S2 images. For each image,
309 clusters of 3 x 3 pixels (900 m^2) were selected from within the seagrass meadow using the
310 following criteria: (i) summer $NDVI_{S2} > 0.67$; (ii) located within a homogeneous area in terms
311 of $NDVI_{S2}$; and (iii) not biased by different tidal heights (Figure A2). According to these
312 criteria, only seagrass-dominated pixels with high summer biomass were selected, and pixels
313 covered by a layer of water during satellite acquisition were avoided. The median $NDVI_{S2}$ and
314 the interquartile range (IQR) were computed from the clusters of each image. The $NDVI_{S2}$
315 time-series was used to assess seasonal seagrass variability in 2018 and in 2019.
316 In order to compare seasonal seagrass changes with those of the background sediment, we
317 also extracted reflectance from bare sediment pixels. Ten 3 x 3 pixel clusters were selected
318 based on the following criteria: (i) summer $NDVI_{S2} < 0.2$; (ii) located in homogeneous areas
319 in terms of $NDVI_{S2}$; and (iii) not biased by different tidal heights (Figure A2). The $NDVI_{S2}$
320 values from seagrass pixels were fit to a Gaussian model to characterize the seagrass growing
321 season and to detect the annual maximum. A criterion of 10% change from the baseline value
322 (i.e., the median of the background pixels in the spring) was used to identify the timing of
323 increasing and decreasing phases (Jönsson and Eklundh, 2004).
324

2.3.4. Comparing S2 with very high-resolution seagrass mapping

To evaluate the representativeness of the S2 pixel size, one very high-resolution WorldView-02 (WV02, pixel size 2 m) scene was acquired over Bourgneuf Bay during low tide for September 27, 2018, and was compared with the S2 image acquired for September 26, 2018. The WV02 scene was delivered orthorectified as top-of-atmosphere radiance. The surface reflectance ($R_{sat\text{-}WV02}$) was obtained using the Fast Line-of-sight Atmospheric Analysis of Hypercubes (FLAASH; Adler-Golden et al., 1998; Anderson et al., 2002) atmospheric correction, available in ENVI 5.0 (Harris Geospatial). As the image was obtained during very clear sky conditions, the atmosphere was modelled using a US standard atmospheric model, with a visibility of 100 km, and a maritime aerosol model that considers the influence of both oceanic winds and the presence of aerosols from terrestrial origins. The performance of the atmospheric correction was assessed using a similar procedure as for S2.

NDVI was computed from $R_{sat\text{-}WV02}$ using the bands centered at 660 and 835 nm ($NDVI_{WV02}$). In order to take the spectral differences between WV02 and S2 into account, $NDVI_{WV02}$ was recalibrated to $NDVI_{S2}$ using our *in situ* hyperspectral library of seagrass reflectance spectra and the SRFs of both sensors (Equation 2).

$$NDVI_{WV02-recalibrated} = 1.0239 \cdot NDVI_{WV02} + 0.0089 \quad \text{Eq. 2}$$

$NDVI_{S2}$ and $NDVI_{WV02\text{-}recalibrated}$ were compared over 100 S2 pixels randomly distributed within the seagrass meadow. For each S2 pixel, a cluster of 5 x 5 WV02 pixels were extracted from the same area (100 m^2). A seagrass percent cover (SPC_{WV02}) map was then computed from $NDVI_{WV02\text{-}recalibrated}$ using the S2 algorithm and masks. Both WV02- and S2-derived seagrass area were compared in order to assess the impact of small-scale spatial variability on

seagrass maps. The comparison was done sequentially for areas covered by an increasing SPC from sparse (20 – 30%) to dense cover (> 90%).

2.4. Statistics for algorithm performance evaluation and map validation

Algorithm performance, *in situ* and satellite product match-ups, and comparison between S2 and WV02 products were evaluated using the regression coefficient of determination (R^2), slope of the linear regression, RMSD (Equation 3), bias (Equation 4), and mean absolute difference (MAD; Equation 5), where N is the number of observations, and x corresponds to modelled or observed data. All statistics were computed using the MATLAB software.

$$\mathrm{RMSD} = \sqrt{\sum_{i=1}^{N} \frac{(x_{\mathrm{modelled},i} - x_{\mathrm{insitu},i})^2}{N-1}} \quad \text{Eq. 3}$$

$$\mathrm{bias} = \sum_{i=1}^{N} \frac{(x_{\mathrm{modelled},i} - x_{\mathrm{insitu},i})}{N} \quad \text{Eq. 4}$$

$$\mathrm{MAD} = \sum_{i=1}^{N} \frac{|x_{\mathrm{modelled},i} - x_{\mathrm{insitu},i}|}{N} \quad \text{Eq. 5}$$

3. Results

3.1. Percent cover and biomass algorithm development

Both seagrass percent cover and biomass were modelled from NDVI (Figure 4) using a linear model (Equation 6; $R^2 = 0.98$; $p < 0.001$, and Equation 7; $R^2 = 0.83$, $p < 0.001$). In order to avoid NDVI saturation, the biomass algorithm was limited to $0.20 \leq \mathrm{NDVI} \leq 0.65$, and pixels with NDVI > 0.65 were assumed to have at least 51.40 g DW m^{-2} of leaf biomass.

$$\mathrm{SPC}_{\mathrm{cores}} = 172.06 \cdot \mathrm{NDVI}_{\mathrm{cores}} - 22.18 \quad \text{Eq. 6}$$

$$SB_{cores} = 91.17 \cdot NDVI_{cores} - 7.86; \text{ for } NDVI_{cores} \leq 0.65 \quad \text{Eq. 7}$$

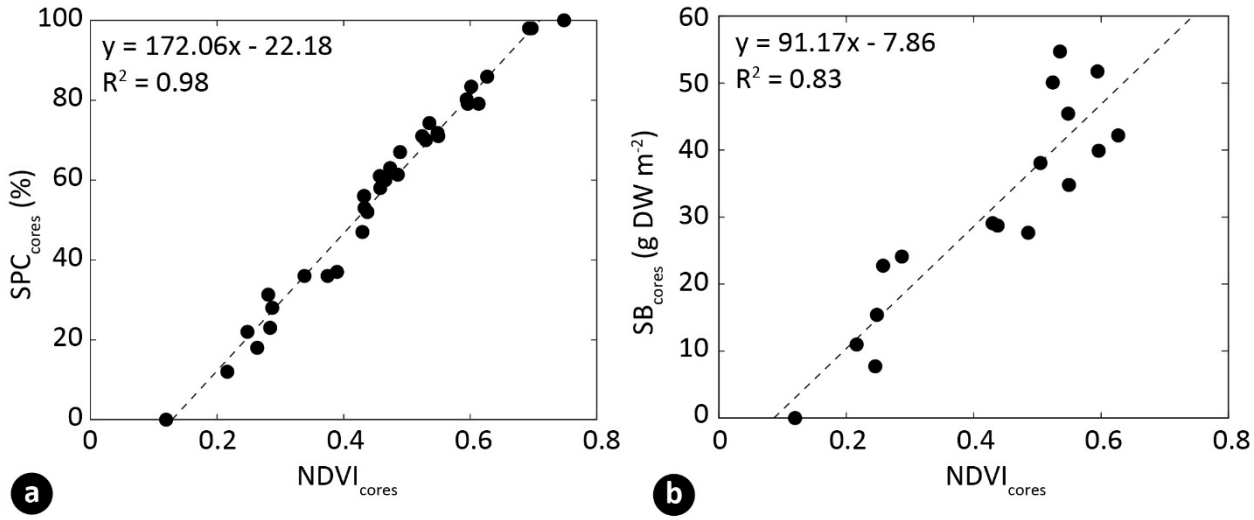

Figure 4.

3.2. Evaluation of percent cover and biomass algorithm performance

The performance of the SPC algorithm was assessed using the independent *in situ* datasets collected from three regions along the European Atlantic coast (Bourgneuf, Marennes-Oléron, and Cadiz Bays). SPC_{cores} was predicted from $NDVI_{cores}$ with very good accuracy (RMSD < 5%, $R^2 \geq 0.98$; Table 2). Performance was consistent across all sites, suggesting that the same algorithm can be used to seamlessly map seagrass cover over a large geographic range, from 36°N (Cadiz Bay) to 47°N (Bourgneuf Bay). Quite good accuracy was also obtained for SB prediction (RMSD = 5.31 g DW m^{-2}, $R^2 = 0.88$; Table 2), despite the limited number (N =12) of samples available for evaluation corresponding to $SB_{cores} \leq 51.4$ g DW m^{-2}.

391 **Table 2.**

Parameter/Dataset	R^2	slope	RMSD	Bias	MAD	N
SPC/Bourgneuf Bay (evaluation set)	0.98	1.00	4.94%	3.69%	3.69%	22
SPC/Marennes-Oléron	0.99	1.06	3.73%	-5.57%	5.71%	28
SPC/Cadiz Bay	0.98	0.92	4.54%	-4.03%	4.97%	24
SB/Bourgneuf Bay (evaluation set)	0.88	0.74	5.31 g DW m^{-2}	-1.54 g DW m^{-2}	5.28 g DW m^{-2}	12

392

393

394 3.3. Satellite-based intertidal seagrass mapping

395 3.3.1. Evaluation of atmospheric correction performance

396 Our results suggest that the performance of the ESA standard atmospheric correction is
397 sufficient for S2 studies of emerged intertidal seagrass meadows (Figure 5). The comparison
398 of the spectral shape and amplitude between $R_{sat\text{-}S2}$ and R_{insitu} showed good agreement,
399 independent of the type of target (i.e., bare sediment, dense seagrass cover, or heterogeneous
400 substrate; Figure 5a and b), with overall good accuracy ($R^2 = 0.971$, $p < 0.001$, RMSD =
401 0.011; Figure 5c). The remaining difference could be attributed to either small-scale spatial
402 variability within a pixel, to field measurement uncertainties (related to, for instance, the time
403 lapse between target and white reference measurements, or to the difference between the
404 satellite instantaneous field-of view (IFOV) and the field measurement viewing angle), and/or
405 to atmospheric correction uncertainties (Thome et al., 2003). Note that the use of a VI based
406 on a band-ratio further minimizes any spectral bias between R_{insitu} and $R_{sat\text{-}S2}$. Over the
407 validation targets, the difference in NDVI between S2 and *in situ* measurements was on the
408 order of 15%.

409

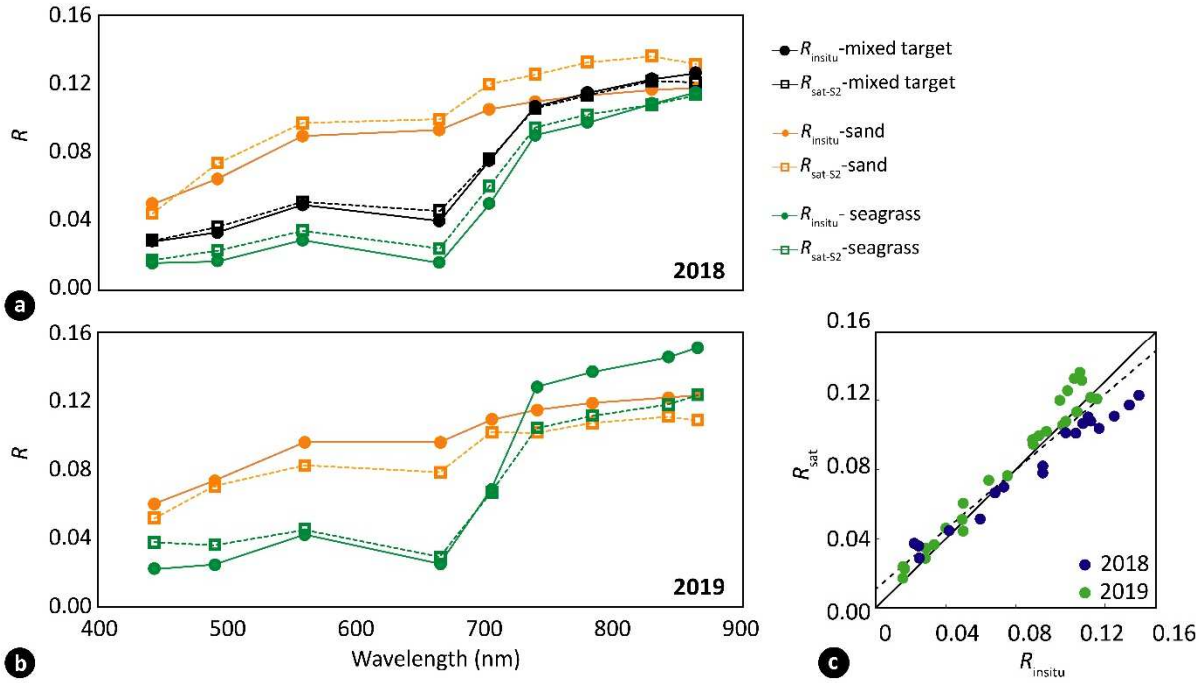

Figure 5.

For WV02, the FLAASH atmospheric correction systematically overestimated the amplitude of the reflectance over the three types of targets, despite preserving overall spectral shape (Figure 6). Note that, in addition to atmospheric correction and field measurement uncertainties, the difference in the date of S2 and WV02 data acquisition may also be responsible for the observed differences between the two products. The consistent overestimation of $R_{\text{sat-WV02}}$ in the red and NIR spectral bands resulted in an underestimation of the NDVI, by approximately 20%.

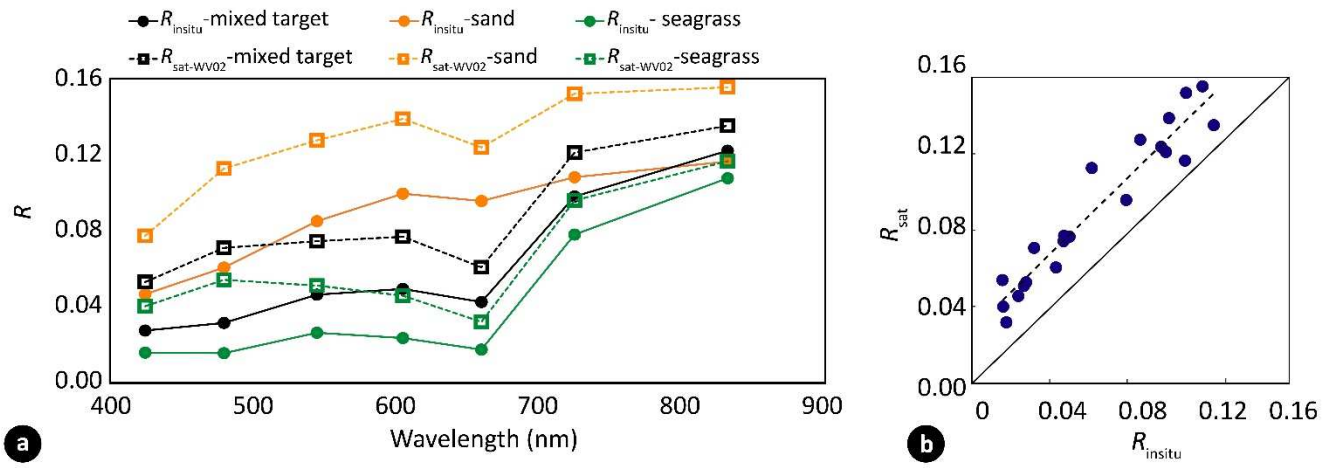

Figure 6.

3.3.2. S2 characterization of the *Z. noltei* seasonal cycle

In Bourgneuf Bay, the $NDVI_{S2}$ exhibited a consistent seasonal cycle characterized by a late summer maximum and a winter minimum (Figure 7). Such a seasonal cycle was expected for this seagrass species in the temperate North Atlantic (Vermaat and Verhagen, 1996). The dataset combined S2 images from two different orbital cycles (#137 and #94) and two sensors (onboard S2A and S2B). We did not observe any significant difference between the orbits or between the sensors, suggesting that the S2 constellation is consistent enough to be combined to characterize the seasonal dynamics of intertidal seagrass meadows. We then applied a Gaussian model to the $NDVI_{S2}$ time-series to better appraise the phenological cycle of *Z. noltei* in Bourgneuf Bay (dashed lines in Figure 7, with $R^2 = 0.93$, $p<0.001$, and RMSD = 0.054 for 2018; and $R^2 = 0.98$, $p<0.001$, and RMSD= 0.028 for 2019). While the number of cloud-free acquisitions was consistently high throughout 2018, in 2019, no cloud-free S2 acquisition was available during low tide after September 29. However, this limited March–September date range seemed sufficient to reconstruct the seasonal cycle based on resulting the Gaussian fit. In both years, the growing season started in mid-May and ended in early-December. The seagrass peak occurred on September 10 ± 3 days in 2018, and on September 4 ± 3 days in 2019. The period of maximum growth was similar in both years, with $NDVI_{S2}$

remaining within 5% of the maximum from August 22 – September 28 in 2018 and from August 14 – September 26 in 2019. Interestingly, the data dispersion was higher in terms of IQR during the increasing and decreasing phases than during the summer maximum, suggesting that the seagrass growth dynamics and decline are spatially heterogeneous within the meadow.

The seasonal variation observed in the Bourgneuf Bay seagrass meadow was compared to that of reference pixels located outside the seagrass-covered area and identified as bare sediment during the summer field observations (black circles in Figure 7). In these background pixels, the annual $NDVI_{S2}$ variation did not exceed 0.24, and was highest in the spring. Such a temporal pattern is consistent with the expected seasonal cycle of benthic microalgae in Bourgneuf Bay (Echappé et al., 2018). From winter to early spring, the $NDVI_{S2}$ time-series of the seagrass meadow was similar to that of the background pixels, suggesting at least a substantial reduction, if not a complete loss, of the above-ground seagrass biomass in the winter. During this period, the NDVI was indeed below the detection limit of sparse seagrass cover, very likely corresponding to benthic diatoms (Barillé et al., 2010).

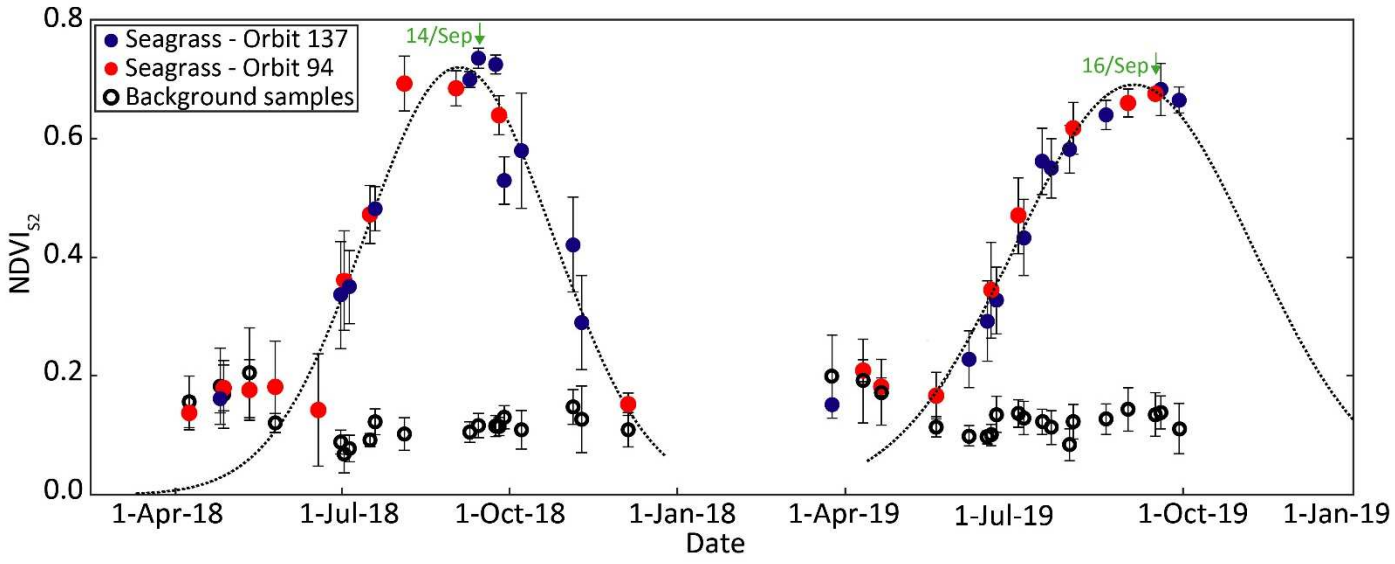

Figure 7.

3.3.3. S2 maps of seagrass percent cover and biomass

Based on our analysis of the seasonal cycle, the S2 scenes captured on September 14, 2018 and September 16, 2019 were selected to compute the seagrass percent cover (SPC_{S2}) and seagrass leaf biomass (SB_{S2}) maps during the seagrass annual maximum. *In situ* SPC measurements available from during the annual peaks in 2018 and 2019 were used to validate the SPC maps. The match-ups showed satisfactory results ($R^2 = 0.79$, $p < 0.001$, RMSD = 14%, bias = -2.09%, and MAD = 10.45%; N = 64), and a linear regression with a slope of 0.94, close to the 1:1 line (Figure 8), was obtained. Relatively limited deviation from this relationship was observed for high percent cover (> 80%), likely due to the spatial homogeneity of dense seagrass patches, whereas the patches of low and intermediate cover were more heterogeneous, thus displaying greater variability. Due to NDVI saturation at high seagrass biomass, it was not possible to estimate leaf biomass beyond a NDVI saturation threshold of 0.65. In the biomass maps presented in Figure 9, pixels with $NDVI_{S2} > 0.65$ were assigned to a class of leaf biomass ≥ 51.4 g DW m^{-2}.

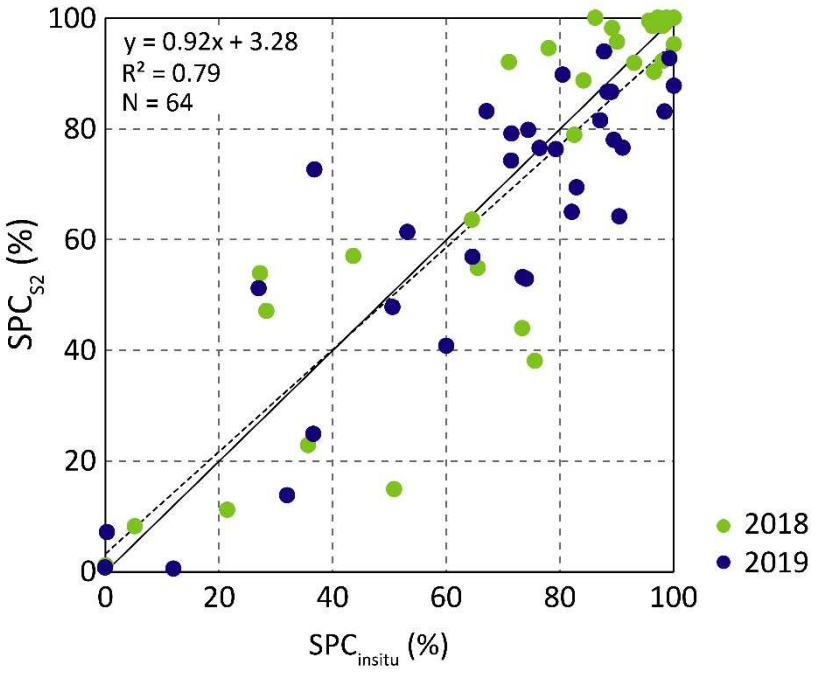

Figure 8.

The S2 seagrass percent cover and biomass maps during the period of annual maximum growth in Bourgneuf Bay are shown in Figure 9. Seagrass distribution showed an elevational pattern, with a marked upper limit at the 4 m LAT isobath close to the shoreline, and a lower limit corresponding to the 2 m LAT isobath. The densest part of the meadow was observed above the 3 m LAT isobath. Superimposed upon the overall vertical zonation, the seagrass spatial distribution also exhibited several small-scale patterns. For example, areas of low SPC that orthogonally streaked the meadow were observed along the tidal channels (Figures 9 and 10; see also photograph in Figure 1c for an *in situ* view).

At a first glance, the overall spatial distribution of *Z. noltei* was more or less similar in 2018 and 2019, with a small increase in the meadow-averaged SPC from one year to the next, from 30.86 ± 29.95 to 33.43 ± 28.16% (non-parametric test on two paired samples = 1.2284e+10, $p < 0.01$), and in SB, from 19.37 ± 15.40 to 21.58 ± 14.87 g DW m^{-2} (non-parametric test on two paired samples = 1.2824e+10, $p < 0.01$). However, while the area of medium to high seagrass cover (SPC ≥ 50%) increased from 2018 (3.02 km^2) to 2019 (3.38 km^2), an opposite trend was observed in the areas of highest seagrass cover and biomass between the two years. For example, the area of densest meadow surface (SPC ≥ 80%) decreased from 1.28 to 0.68 km^2 between 2018 and 2019. Similarly, the surface area of biomass ≥ 51.4 g DW m^{-2} decreased from 0.74 to 0.15 km^2 between 2018 and 2019. Although investigating the causes underlying this interannual variability was beyond the scope of the present study, these detailed maps demonstrate the ability of S2 to quantitatively monitor spatio-temporal changes in seagrass distribution, enabling such investigation in future works.

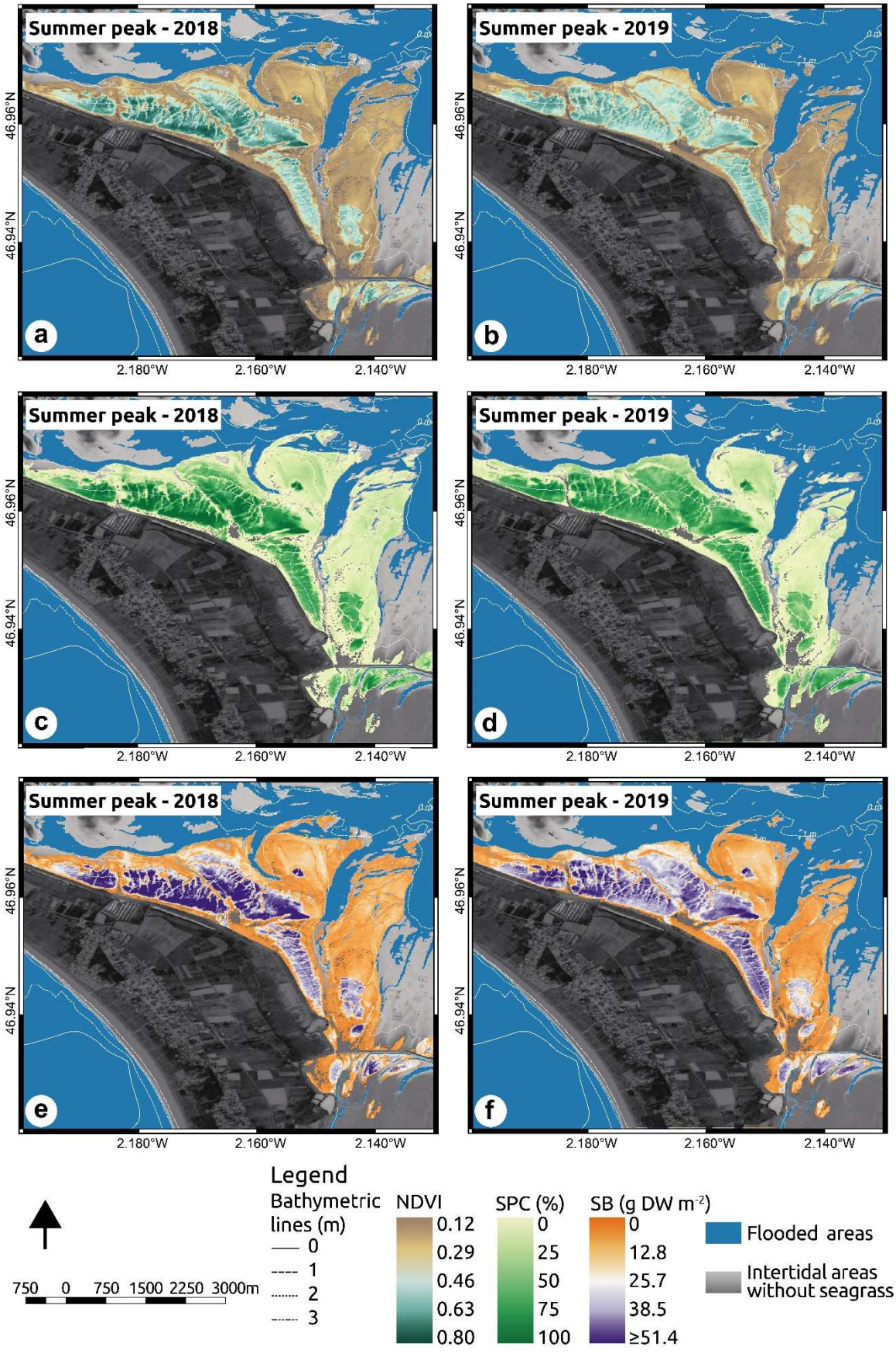

499

500 **Figure 9.**

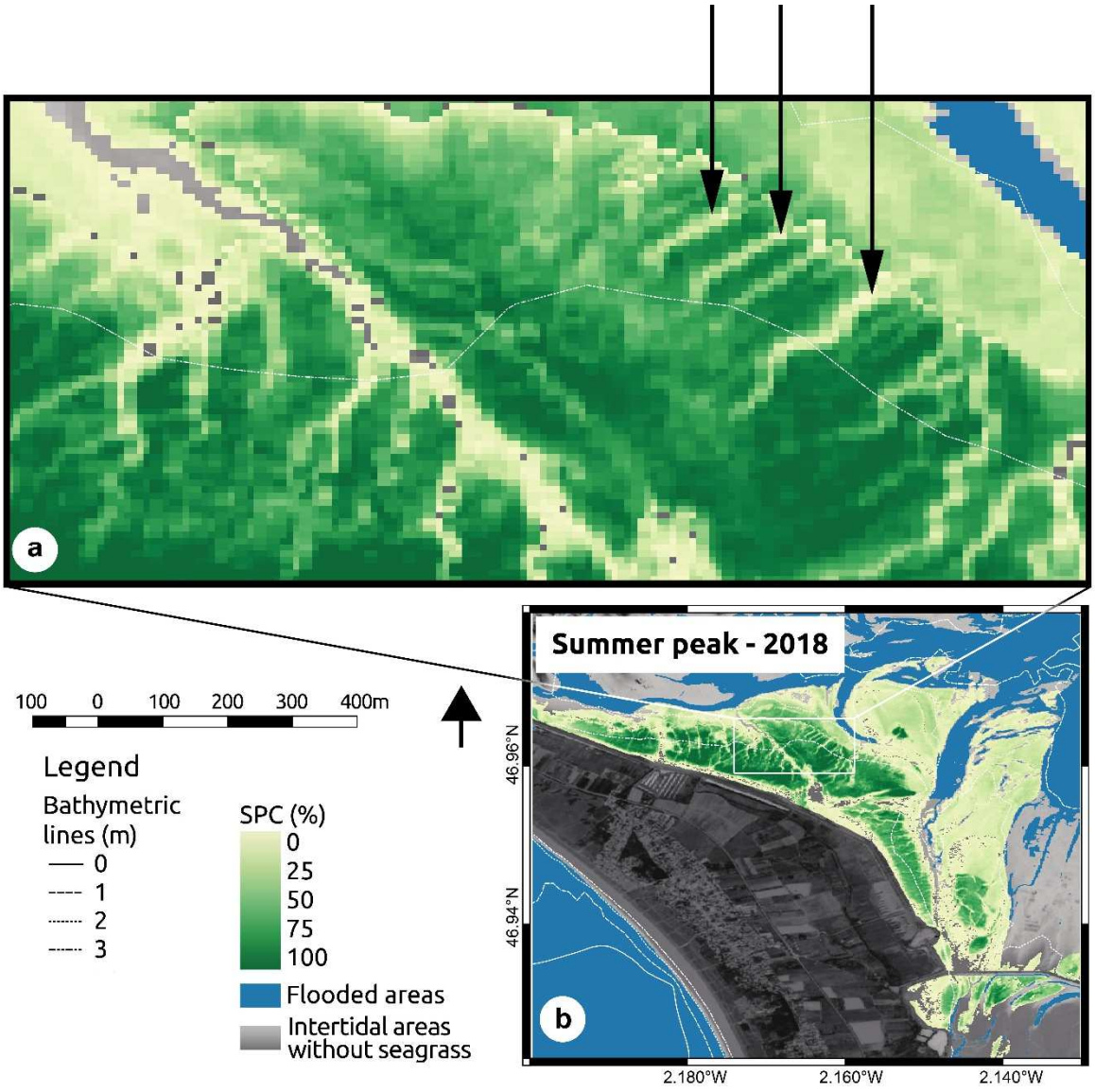

Figure 10.

Besides providing valuable interannual observations, S2 also makes it possible to study the seasonal variability in seagrass spatial distribution. Selected examples of SPC maps are shown at different phases of the seasonal cycle (Figure 7) to illustrate the variations in spatial patterns observed throughout the year (Figure 11). A striking difference is observed between early spring (Figure 11a) and early summer (Figure 11b). This example illustrates the rapid dynamic of seagrass development, from a roughly bare surface to an established meadow covering 5.18 km^2 (SPC $\geq$ 20%) three months later. Even if some areas displayed specific

temporal dynamics, an overall synchronicity prevailed in the establishment of the summer meadow. Then, while the meadow's extension and spatial patterns were roughly the same from mid-July to the end of September, the density of the cover varied significantly throughout the summer period, with a clear SPC maximum in mid-September (Figure 11g-i). Even if the overall spatial structure did not significantly change from mid- to the end of September, a decline in SPC was already noticeable (mostly in the western part of the meadow), with a decrease in the densest areas (SPC > 50%), from 3.02 to 2.57 km^2, within only two weeks (Figure 11c, d). The meadow then rapidly declined, and by mid-December the above-ground cover had almost completely disappeared in most parts of the meadow (Figure 11e). While a more quantitative analysis of the yearly changes in seagrass spatial patterns (as done, for example, in Echappé et al., (2018) and Daggers et al., (2020) for microphytobenthos) is out of the scope of the present study, these selected examples nonetheless demonstrate the interest of spatial-rich and highly-resolute S2 time-series for macroscale studies of seagrass landscape dynamics.

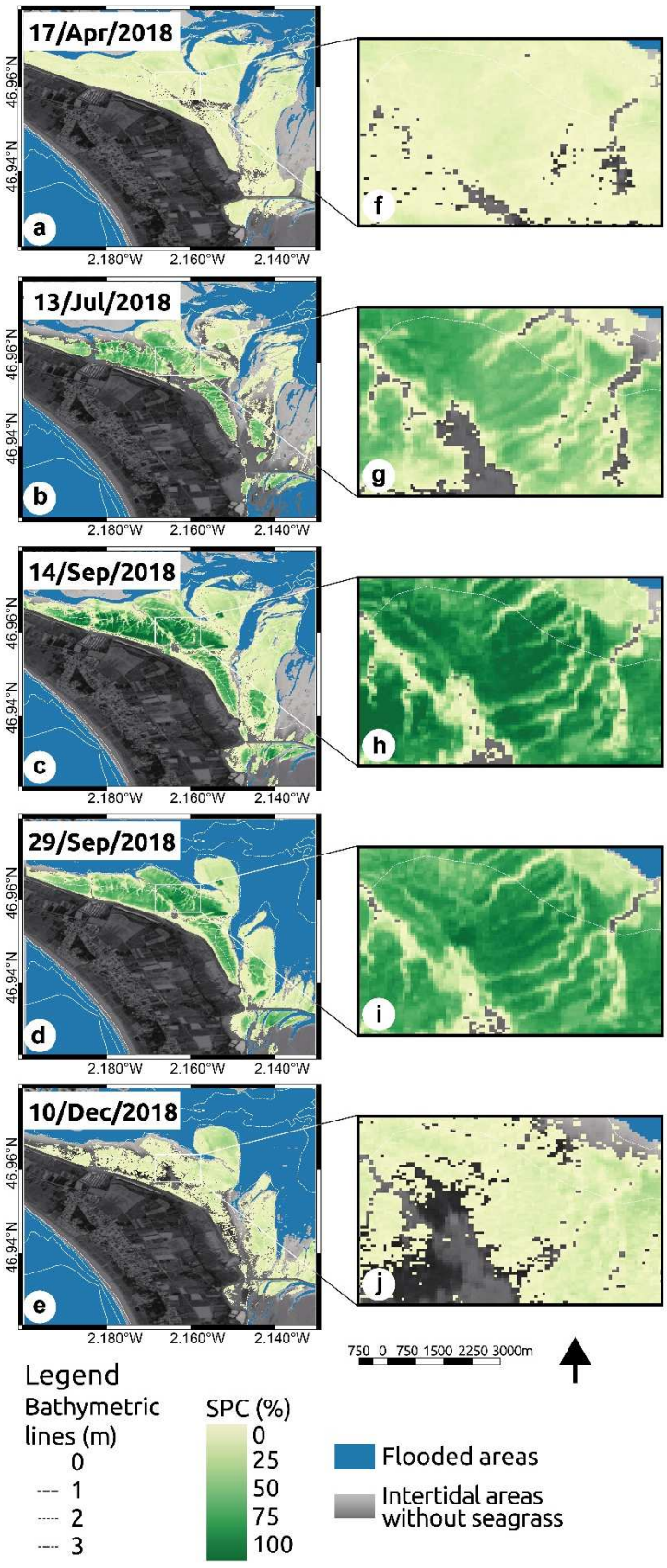
17/Apr/2018
13/Jul/2018
14/Sep/2018
29/Sep/2018
10/Dec/2018
a
b
c
d
e
f
g
h
i
j
46.96°N
46.94°N
2.180°W
2.160°W
2.140°W
750 0 750 1500 2250 3000m
Legend
Bathymetric lines (m)
0
1
2
3
SPC (%)
0
25
50
75
100
Flooded areas
Intertidal areas without seagrass

Figure 11.

561 3.3.4 Comparing S2 with very high-resolution seagrass mapping

562 The S2-WV02 comparison showed an overall agreement (R^2 = 0.78, N = 100, p< 0.001,

563 RMSD = 0.073) despite underestimation by $NDVI_{WV02\text{-}recalibrated}$ (Figure 12a). While the NDVI

564 underestimation was consistent with the WV02 reflectance overestimation (Figure 6), it could

565 also be attributed to differences in viewing angles and/or spatial resolutions of the two

566 sensors. The difference in NDVI also influenced the computation of seagrass cover, and

567 associated surface area estimations. The SPC_{S2} areas were systematically larger than the

568 SPC_{WV02} areas (Figure 12b). This overestimation was lower in dense areas (SPC ≥ 50%) than

569 in sparse areas where the number of small and fragmented seagrass patches is expected to

570 smooth out $NDVI_{S2}$ due to the difference in spatial resolution (i.e. the same surface of 100 m^2

571 corresponds to 1 S2 pixel *vs.* 25 WV02 pixels).

572 Despite the aforementioned differences, the spatial distribution of SPC_{S2} and SPC_{WV02}

573 presented similar patterns (Figure 13), diverging mainly in the detection of small-scale

574 features such as narrow tidal channels, which were not detected by S2, and in noise level,

575 which was higher for WV02 due to its higher spatial resolution.

576

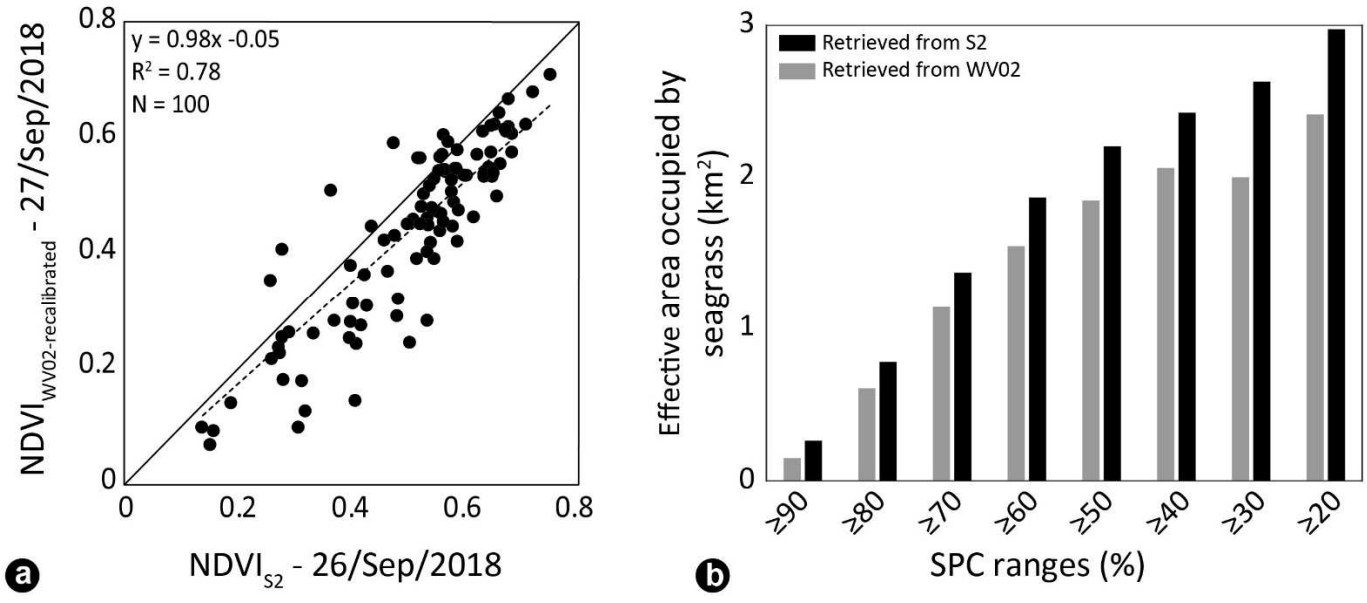

577

578 **Figure 12.**

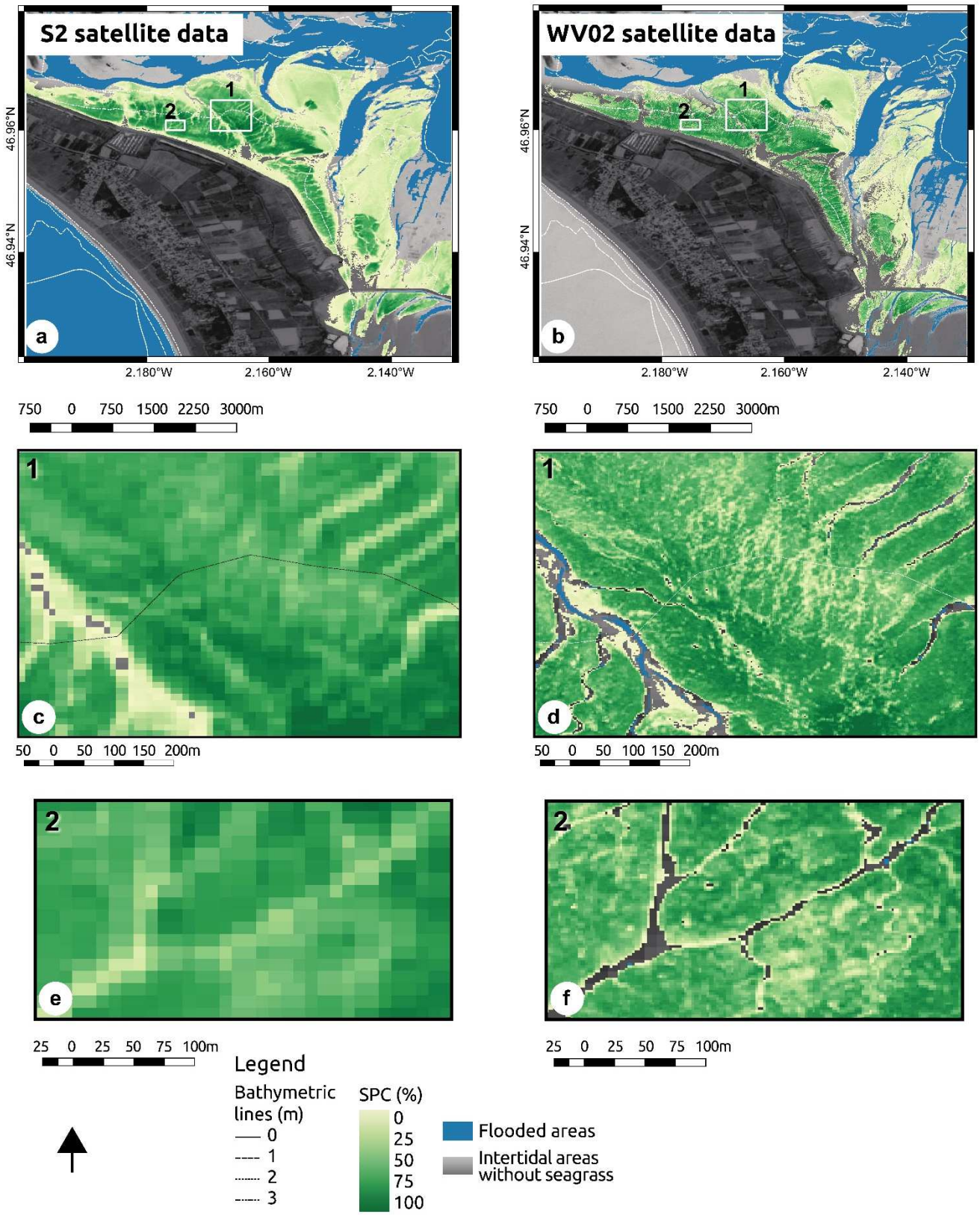
S2 satellite data
WV02 satellite data
1
2
a
b
c
d
e
f
46.96°N
46.94°N
2.180°W
2.160°W
2.140°W
750 0 750 1500 2250 3000m
50 0 50 100 150 200m
25 0 25 50 75 100m
Legend
Bathymetric lines (m)
0
1
2
3
SPC (%)
0
25
50
75
100
Flooded areas
Intertidal areas without seagrass

Figure 13.

582 **4. Discussion**

583 Describing the spatial distribution of seagrass meadows is important for the monitoring and
584 management of this protected habitat. In the present study, we showed that S2 data can be
585 used to describe the spatio-temporal dynamics of *Zostera noltei* intertidal meadows. Seagrass
586 percent cover and leaf biomass were the two biological descriptors that were remotely-sensed,
587 with strengths and limitations that will be discussed in the next sections.

588

589 4.1. Seagrass percent cover and leaf biomass

590 In this study, the ubiquitous NDVI was chosen from among different VIs to retrieve two
591 biological descriptors of seagrass communities: percent cover and leaf biomass. The NDVI
592 has been broadly demonstrated to be a good descriptor of vegetation dynamics for many types
593 of ecosystems, including wetlands (e.g., Doughty and Cavanaugh, 2019; Echappé et al., 2018;
594 Pettorelli et al., 2005; Prabhakara et al., 2015; Zoffoli et al., 2008). Previous works on
595 intertidal seagrass remote sensing reported a quasi-linear relationship between NDVI and *Z.*
596 *noltei* percent cover (Valle et al., 2015), supporting the SPC-NDVI relationship observed in
597 our work. A linear regression between NDVI and percent cover was also observed for a
598 variety of terrestrial crops (Prabhakara et al., 2015).

599 The validation of our SPC algorithm suggests that the empirical SPC-NDVI relationship
600 found in this work is intrinsic to *Z. noltei*, but independent of time and region, and thus
601 applicable to other intertidal systems dominated by this species. The SPC maps were
602 validated with *in situ* SPC measurements, with match-ups showing a RMSD of 14%. Errors in
603 geolocation and intrapixel heterogeneity (such as the presence of puddles) may have
604 contributed to the differences found between *in situ* and satellite data. The limitation of the
605 equations proposed here to compute the biological descriptors is that they can only be applied
606 with high accuracy during the summer maximum, and in meadows dominated by *Z. noltei*.

607 Seasonal changes in pigment concentration and composition have previously been described
608 for *Z. noltei* (Bargain et al., 2013). These are expected to have an effect on the spectral
609 response and, therefore, on the NDVI. Due to this, different relationships between seagrass
610 biological descriptors and NDVI are expected in the spring and in the fall.
611 The biomass descriptor was more difficult to develop for two reasons: first, it had a non-linear
612 relationship with NDVI, but this saturation with increasing biomass was expected (Bargain et
613 al., 2012). Secondly, we did not collect validation samples, which would be destructive (i.e.,
614 removing seagrass from large areas). The latter constraint may be partly overcome using
615 unmanned aerial vehicles (UAV), which can acquire images with a spatial resolution on the
616 order of centimeters (2-5 cm) (Duffy et al. 2018). Biomass could then be sampled from
617 smaller surfaces, allowing map validation with a much more limited impact (Sani et al.,
618 2019). A different challenge for remote sensing techniques is the estimation of below-ground
619 biomass (BGB), as reflectance only provides information on above-ground data. This is an
620 important issue, since previous authors have pointed out that a significant proportion of
621 carbon reserves is stored in BGB in seagrass ecosystems, and blue carbon assimilation models
622 require this information (Sani et al., 2019). Previous works have reported highly variable
623 AGB/BGB ratios between species and sites, highlighting the need for additional core
624 sampling to obtain site-specific AGB/BGB ratios (Githaiga et al., 2017; Postlethwaite et al.,
625 2018) so as to model BGB from AGB estimates.
626
627 4.2. S2 capabilities for seagrass mapping
628 The application of the SPC algorithm based on $NDVI_{S2}$ allowed the highest spatial resolution
629 offered by S2 to be used, producing SPC maps at a pixel size of 10 m. Comparing satellite-
630 derived SPC at different spatial resolutions (i.e., 10 *vs.* 2 m) showed that the pixel size of S2
631 is sufficient to accurately describe the overall spatial distribution of intertidal *Z. noltei*

meadows, making temporally-robust (i.e., frequent revisit time) seagrass indicator monitoring possible to implement at no-cost. We also compared the pixel size of S2 with that of Landsat8 (L8; 30 m) (figure not shown). We observed that some geomorphological features, such as tidal channels, could not be detected at this 30 m pixel size (Hedley et al., 2016), whereas they are visible on the S2 maps (Figure 13). Therefore, in this study, 10 m was found to be an appropriate pixel size to observe meadows covering several square kilometres, although Landsat may remain useful for meadows covering hundreds of square kilometres or even to follow temporal trends in the overall state of the meadow (Ward et al., 1997).

The French Bourgneuf Bay study site benefited from the overlap of two S2 orbits at this study site, reducing the revisit time from 5 to 2-3 days. This doubles the number of images produced for this area, allowing a satisfactory sample size after applying the tidal height and cloud cover restrictions (Hedley et al., 2016; Hestir et al., 2015). Even when only ~20% of the scenes were suitable for the application of our algorithms, the number of scenes was sufficient to characterize the seasonal cycle of *Z. noltei* and to select the best images during the maximum annual peak, since the seasonal variability revealed in this work matched the unimodal seasonal pattern previously described for this species along western European coasts (Perez-Llorens and Niell, 1993, Vermaat and Verhagen, 1996, Peralta et al, 2005). This seasonal pattern has mainly been attributed to seasonal patterns in temperature and daily light availability (Soissons et al., 2018). A detailed phenological analysis was beyond the scope of this work, which instead demonstrates the potential of S2 for seasonal seagrass studies at the pan-European level.

Both the annual variation in sun elevation and the orbital difference in the sensor view geometry can influence measured reflectance due to the anisotropy of the observed target. This is defined by its bidirectional reflectance distribution function (BRDF), which depends on the type of target. Over terrestrial vegetation, the directional effects are generally lower

than 6% (Vermote et al., 2009). Consequently, a low BRDF effect is expected for intertidal areas, since areas covered by water were excluded in this work. Interestingly, NDVI is less impacted by anisotropy effects than single-band reflectance, because the directional difference is similar in the red and NIR spectral regions (Roy et al., 2017), minimizing its influence on the band ratio index (Bréon and Vermote, 2012; Vermote et al., 2009). In our $NDVI_{S2}$ time-series, there was no significant orbital bias for pixels with 100% seagrass cover, nor for bare sediment pixels (i.e., 0% seagrass cover). In summary, S2 can be considered to be a robust tool for monitoring intertidal seagrass beds due to its sufficient revisit time, viewing angle, and spatial resolution, as well as the quality of the ESA standard atmospheric correction.

4.3. Characterization of seasonal variability: a prerequisite to interannual comparison

Interannual studies of seagrass dynamics require seasonal variability to be taken into account, since only images from within the same season can be consistently analyzed without artificially creating temporal bias (Roelfsema et al., 2013). This is especially important for high turnover species, such as *Z. noltei* (Peralta et al., 2005), which can explain the drastic change in both NDVI and percent cover observed between September 14 and 29, 2018 (Figure 11c-d), when the dense meadow area (SPC ≥ 50%) decreased from 3.02 to 2.57 km^2, with a greater change in the western area than in the eastern one. Such a rapid change is remarkable and can mainly be explained by changes in vegetation state. Additionally, for interannual studies, it is recommended to focus on the maximum growth period, since the spatial variability of the NDVI is lower than during increasing and decreasing phases (see IQR in Figure 7).

Nevertheless, key dates of the seasonal cycle may fluctuate between years. Therefore, the seasonal cycle should be characterized on a year-by-year basis to determine which scene corresponds to the seasonal maximum. The influence of the seasonal cycle is expected to have

682 a latitudinal pattern, probably being less at lower latitudes, where the seasons themselves are
683 less pronounced (Lyons et al., 2013) than at higher latitudes. In any case, this source of
684 variability merits further investigation.
685
686 4.4. Water level considerations
687 Water molecules have high absorption in the red and IR spectral regions. For this reason, the
688 spectral reflectance spectrum of an intertidal object varies drastically with degree of emersion.
689 In a macrotidal environment, the tidal variability can significantly impact the spatio-temporal
690 distribution of remotely-sensed parameters, such as seagrass NDVI, and, consequently, SPC.
691 Figure 14 illustrates these effects, as the estimate of the whole meadow surface area
692 (corresponding to $0.12 \leq NDVI \leq 0.8$) decreased from 11.6 km^2 on September 1 to 4.15 km^2
693 on September 11, 2019, due to contrasting tidal heights (0.24 *vs.* 3.25 m LAT). In conclusion,
694 we recommend the selection of images with as low a water level as possible so as to
695 maximize the area able to be mapped. The maximum tidal height that allows seagrass
696 meadows to be mapped using satellite data necessarily requires prior knowledge of the area,
697 as it depends on the tidal amplitude, bathymetry/elevation, and location of the seagrass
698 meadow itself.

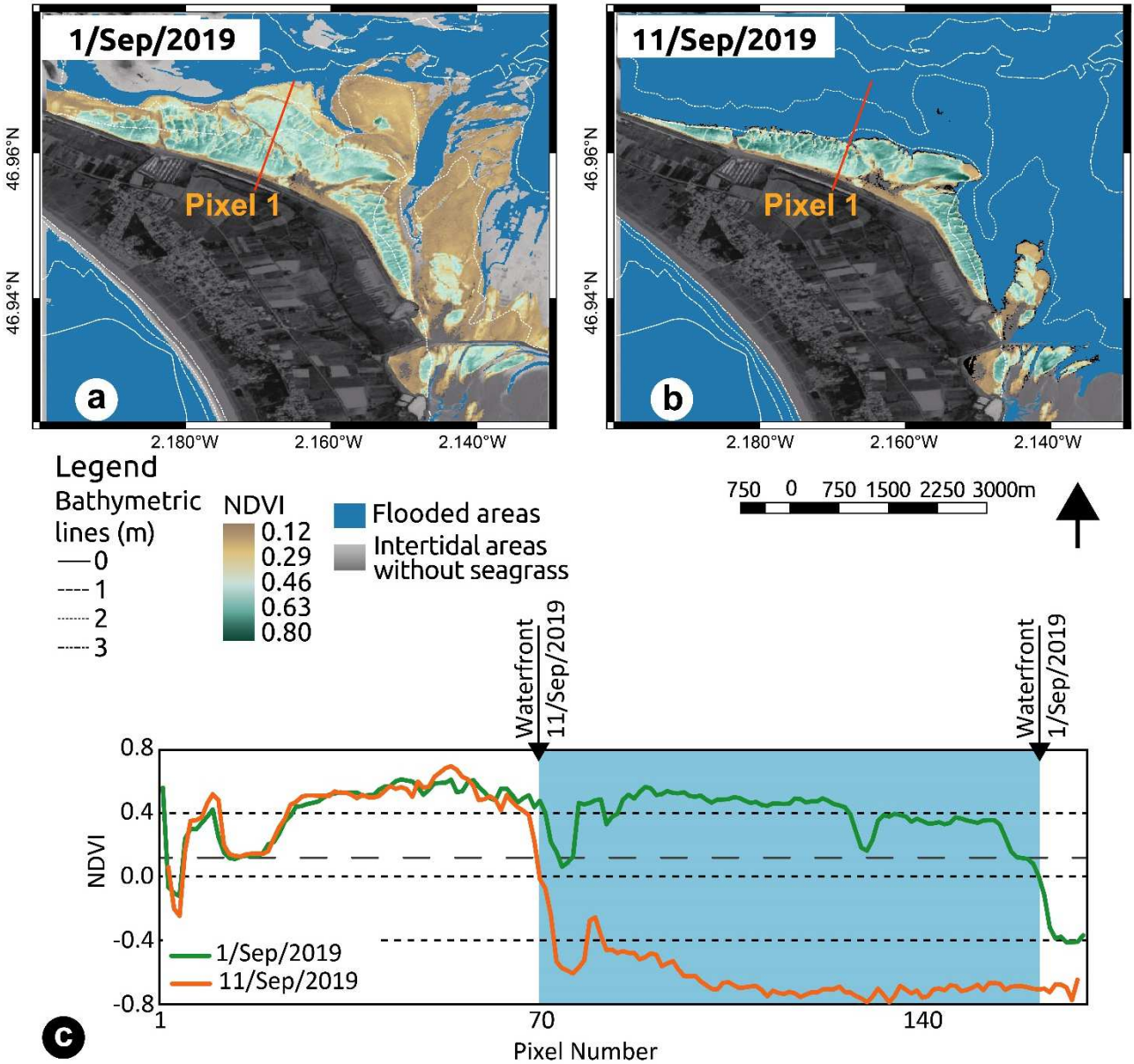

699 **Figure 14.**

700

701 4.5. Recommendations for an areal extent metric

702 A relevant variable to characterize the status of seagrass ecosystems is the total area of the
703 meadow. This is used by the European Water Framework Directive (WFD) to evaluate the
704 quality of coastal waters (Papathanasopoulou et al., 2019), and is usually a key parameter
705 used to detect temporal trends. Estimation of the total area of a seagrass meadow therefore
706 needs to make use of the most robust calculations possible (i.e., be subject to the lowest
707 possible uncertainties, as incorrect estimates can lead to inappropriate management). Remote

sensing, with its synoptic coverage, can provide lower cost and less time-consuming surface estimates compared with traditional field techniques. However, remote sensing data are also characterized by a number of uncertainties in intertidal meadows. As we saw from the comparison between SPC from S2 and WV02, the areas associated with the greatest uncertainty in terms of spatial resolution were those where SPC < 50%. The background contribution is also lower for SPC ≥ 50%, and the debatable issue of using a lower threshold used to distinguish bare sediment from seagrass meadow with low percent cover can be avoided. We therefore suggest adding two surface metrics based on seagrass areas with SPC ≥ 50% and SPC ≥ 80 % to estimate the interannual variation in the areal extent of the meadow. The choice of a surface metric impacts the ecological status assigned by the European WFD (see for example case study #2 in Papathanasopoulou et al., 2019), and the plasticity of remote sensing data makes it possible to consistently investigate different metrics and indicators.

In a previous study based on the analysis of SPOT images to assess the areal extent of the seagrass meadow, Barillé et al. (2010) observed an overall increase in the seagrass beds in Bourgneuf Bay over a 15-year period from 1991 to 2005. They also reported dramatic and rapid variation in the meadow's surface area between 1996 and 1998. In the present study, the total surface of the seagrass meadow in 2018 and 2019 was comparable with the largest surface of the 1991 – 2005 time-series. However, in such a highly dynamic ecosystem (Philippart and Dijkema, 1995; Charpentier et al., 2005), we cannot infer the trajectory of the seagrass meadows in between. Completing the 12-year gap (2006 – 2017) with SPOT and/or Landsat archive imagery will allow the analysis of the interannual variability based on images acquired during the season of maximum development. However, due to the limited number of historical images per year, the seasonal cycle cannot be described with the same temporal resolution as we have done with S2 in this work (see paragraph 4.3). Despite this possible

source of variability, an interesting perspective would be to construct a 30-year time-series (1990 – 2020) starting with SPOT imagery (Barillé et al., 2010) and continuing with S2 (this study), all the more as this kind of continuity was expected from the launch of the S2 mission (Hagolle et al., 2015). Such a spatially-rich and long-term time-series could represent a valuable dataset for environmental management programs, such as the European WFD (Papathanasopoulou et al., 2019).

4.6. Recommendation for multi-sensor NDVI time-series

To obtain NDVI time-series spanning two or three decades, different multispectral sensors must be used and intercalibrated. The S2 time-series is limited by the recent launch of S2A in 2015, and a longer revisit time prior to the launch of S2B in 2017. Longer and/or more complete NDVI time-series could be obtained from historical and on-going satellite missions such as SPOT, Landsat, or Worldview. With all of them, it is possible to calculate the NDVI, but at different spatial and spectral resolutions; hence they are not equally suitable. In such cases, sensor inter-calibration is required. Since the spectral response functions impact the red and NIR values, we provide a parameterization to rescale the NDVI from several multispectral missions (SPOT, L8, Worldview2, Pléiades, Quickbird, and Ikonos) to S2 (Table 3). These parameterizations were obtained from our hyperspectral *in situ* dataset by simulating NDVI values for different sensors using their respective SRF (Cundill et al., 2015; González-Audícana et al., 2006; USGS, 2018). For consistency with a previous study based on the long-term analysis of SPOT imagery (Barillé et al., 2010), we redefined the NDVI thresholds to distinguish two classes of seagrass cover: sparse cover ($20\% < SPC < 50\%$) and dense cover ($SPC \geq 50\%$), and provided consistent thresholds for all sensors (Table 4). To complement the NDVI inter-calibration, the difference in the acquisition geometry of each sensor has to be taken into account. For example, the differences between the field-of-view of

S2 and L8 (20.6° and 15° respectively) need to be compensated through BRDF modelling (Claverie et al., 2018). Moreover, to reduce processing uncertainties, the same type of atmospheric correction should be applied whenever possible (Barnes et al., 2014).

Table 3.

Sensor	m	b
SPOT1	1.0574	0.0246
Landsat-8	0.9915	0.0076
Worldview2	1.0239	0.0089
Pléiades	1.1035	0.0076
Quickbird	1.0993	0.0186
Ikonos	1.2022	0.0182

Table 4.

	Seagrass cover	
Mission	**Sparse**	**Dense**
Sentinel-2	0.25 - 0.42	0.42 - 0.80
SPOT1	0.21 - 0.37	0.37 - 0.73
Landsat-8	0.24 - 0.42	0.42 - 0.80
Worldview2	0.24 - 0.40	0.40 - 0.77
Pléiades	0.22 - 0.37	0.37 - 0.72
Quickbird	0.21 - 0.37	0.37 - 0.71
Ikonos	0.19 - 0.33	0.33 - 0.65

5. Conclusions

In this work, we developed and validated algorithms to estimate seagrass percent cover (SPC) and seagrass leaf biomass (SB) from Sentinel-2 (S2) remote sensing data. These algorithms were derived using *in situ* measurements made in *Z. noltei*-dominated meadows in multiple years and locations. The geographic extent of our sampling makes the algorithms applicable from North Africa to North Europe, where *Z. noltei* occurs. The detailed description of algorithm development and assessment also sets guidelines to easily adapt the algorithm to meadows dominated by other species, as long as the emerged seagrasses can be observed during low-tide. The performance of S2 intertidal seagrass meadow mapping at a pixel size of 10 m was estimated with a RMSD of 14%. Such a spatial resolution enabled the observation of characteristic features of the meadow, also revealed in 2 m spatial resolution maps from WV02 that allowed the monitoring of patch dynamics within the meadow. Valuable information about seasonal seagrass dynamics was also able to be obtained due to the frequent S2 revisit time, and it was possible to characterize the seasonal cycle of the seagrass meadow for two consecutive years on a refined time-scale. At the French Bourgneuf Bay case study site, the *Z. noltei* seasonal cycle was characterized by a growing season from mid-May to the beginning of December, a late-summer maximum, and a winter minimum, matching the overall temporal variation found from previous works based on *in situ* observations. Future work of interest would be the automated retrieval of the phenological parameters developed here to study interannual changes over a broader geographic scale to evaluate latitudinal patterns in phenology. Since images may be from any time within a given temporal window around the peak of maximum development depending on availability and suitability (i.e., ± 15 days), and because of the influence of water height on the interpretation of low tide images, our results call for caution in satellite image selection for this intertidal habitat, providing instructions to perform unbiased studies. The S2 dataset is quite recent, but could be

794 complemented by multispectral satellite time-series to investigate long-term changes in
795 seagrass dynamics. For this purpose, we provide guidelines to inter-calibrate a multi-sensor
796 NDVI database, and recommend the application of consistent atmospheric correction, if
797 possible, so as to avoid instrumental biases and misinterpretation of temporal changes.
798
799 **References**

800 Adler-Golden, S.; Berk, A.; Bernstein, L.S.; Richtsmeier, S.; Acharya, P.K.; Matthew, M.W.;
801 Anderson, G.P.; Allred, C.L.; Jeong, L.S.; Chetwynd, J.H. FLAASH, a MODTRAN4
802 atmospheric correction package for hyperspectral data retrievals and simulations. In
803 Procedings of the 7th Annual JPL Airborne Earth Science Workshop, Pasadena, CA,
804 USA, 12–16 January 1998; Green, R.O., Ed.; pp. 9–14.
805 Anderson, G.P.; Felde, G.W.; Hoke, M.L.; Ratkowski, A.J.; Cooley, T.W.; Chetwynd, J.H.,
806 Jr.; Gardner, J.A.; Adler-Golden, S.M.; Matthew, M.W.; Berk, A.; et al. MODTRAN4-
807 based atmospheric correction algorithm: FLAASH (fast line-of-sight atmospheric
808 analysis of spectral hypercubes). In Algorithms and Technologies for Multispectral,
809 Hyperspectral, and Ultraspectral Imagery VIII (Proceedings of SPIE); Shen, S.S.,
810 Lewis, P.E., Eds.; Society of Photo Optics: Orlando, FL, USA, 2002; pp. 65–71
811 Barbier, E.B., Hacker, S.D., Kennedy, C.J., Koch, E.W., Stier, A.C., Silliman, B.R., 2011.
812 The value of estuarine and coastal ecosystem services. Ecol. Monogr. 81, 169–193.
813 https://doi.org/10.1890/10-1510.1
814 Bargain, A., Robin, M., Le Men, E., Huete, A., Barillé, L., 2012. Spectral response of the
815 seagrass *Zostera noltii* with different sediment backgrounds. Aquat. Bot. 98, 45–56.
816 https://doi.org/10.1016/j.aquabot.2011.12.009
817 Bargain, A., Robin, M., Méléder, V., Rosa, P., Le Menn, E., Harin, N., Barillé, L., 2013.
818 Seasonal spectral variation of *Zostera noltii* and its influence on pigment-based

819 Vegetation Indices. J. Exp. Mar. Bio. Ecol. 446, 86–94.
820 https://doi.org/10.1016/j.jembe.2013.04.012
821 Barillé, L., Robin, M., Harin, N., Bargain, A., Launeau, P., 2010. Increase in seagrass
822 distribution at Bourgneuf Bay (France) detected by spatial remote sensing. Aquat. Bot.
823 92, 185–194. https://doi.org/10.1016/j.aquabot.2009.11.006
824 Barnes, B.B., Hu, C., Holekamp, K.L., Blonski, S., Spiering, B.A., Palandro, D., Lapointe, B.,
825 2014. Use of Landsat data to track historical water quality changes in Florida Keys
826 marine environments. Remote Sens. Environ. 140, 485–496.
827 https://doi.org/10.1016/j.rse.2013.09.020
828 Borum, J., Sand-jensen, K., 2019. Nordic Society Oikos Is Total Primary Production in
829 Shallow Coastal Marine Waters Stimulated by Nitrogen Loading? Author(s): Jens
830 Borum and Kaj Sand-Jensen Published by: Wiley on behalf of Nordic Society Oikos
831 Stable URL : https://www.jstor.org/stabl 76, 406–410.
832 Bréon, F.M., Vermote, E., 2012. Correction of MODIS surface reflectance time series for
833 BRDF effects. Remote Sens. Environ. 125, 1–9.
834 https://doi.org/10.1016/j.rse.2012.06.025
835 Burdick, D., Kendrick, G., 2001. Standards for seagrass collection, identification and sample
836 design. In Global Seagrass Research Methods F.T. Short & R.G Cole (Eds.), Elsevier
837 Science B.V., 79-100.
838 Calleja, F., Galvan, C., Silio-Calzada, A., Juanes, J.A., Ondiviela, B., 2017. Long-term
839 analysis of *Zostera noltei*: A retrospective approach for understanding seagrasses'
840 dynamics. Mar. Environ. Res. 130, 93–105.
841 Charpentier, A., Grillas, P., Lescuyer, F., Coulet, E., Auby, I., 2005. Spatio-temporal
842 dynamics of a *Zostera noltii* dominated community over a period of fluctuating salinity

in a shallow lagoon, Southern France. Estuar. Coast. Shelf Sci. 64, 307–325. https://doi.org/10.1016/j.ecss.2005.02.024

Claverie, M., Ju, J., Masek, J.G., Dungan, J.L., Vermote, E.F., Roger, J.-C., Skakun, S. V., Justice, C., 2018. The Harmonized Landsat and Sentinel-2 surface reflectance data set. Remote Sens. Environ. 219, 145–161. https://doi.org/10.1016/j.rse.2018.09.002

Costanza, R., D'Arge, R., de Groot, R., Farber, S., Grasso, M., Hannon, B., Limburg, K., Naeem, S., O'Neill, R. V., Paruelo, J., Raskin, R.G., Sutton, P., van den Belt, M., 1997. The value of the world's ecosystem services and natural capital. LK - https://royalroads.on.worldcat.org/oclc/4592801201. Nature 387, 253–260.

Cundill, S.L., der van Werff, H.M.A., der van Meijde, M., 2015. Adjusting spectral indices for spectral response function differences of very high spatial resolution sensors simulated from field spectra. Sensors (Switzerland) 15, 6221–6240. https://doi.org/10.3390/s150306221

Daggers, T. D., Herman, P. M., Van Der Wal, D., 2020. Seasonal and spatial variability in patchiness of microphytobenthos on intertidal flats from Sentinel-2 satellite imagery. Front. Mar. Sci. https://doi.org/10.3389/fmars.2020.00392

Dekker, A.G., Brando, V.E., Anstee, J.M., 2005. Retrospective seagrass change detection in a shallow coastal tidal Australian lake. Remote Sens. Environ. 97, 415–433. https://doi.org/10.1016/j.rse.2005.02.017

Dewsbury, B.M., Bhat, M., Fourqurean, J.W., 2016. A review of seagrass economic valuations: Gaps and progress in valuation approaches. Ecosyst. Serv. 18, 68–77. https://doi.org/10.1016/j.ecoser.2016.02.010

Diaz-Pulido, G., Gouezo, M., Tilbrook, B., Dove, S., Anthony, K.R.N., 2011. High CO2 enhances the competitive strength of seaweeds over corals. Ecol. Lett. https://doi.org/10.1111/j.1461-0248.2010.01565.x

868 Doughty, C.L., Cavanaugh, K.C., 2019. Mapping Coastal Wetland Biomass from High
869 Resolution Unmanned Aerial Vehicle (UAV) Imagery. Remote Sens. 11.
870 https://doi.org/10.3390/rs11050540
871 Duarte, C.M., 1995. Submerged aquatic vegetation in relation to different nutrient regimes.
872 Ophelia 41, 87–112. https://doi.org/10.1080/00785236.1995.10422039
873 Duffy, J.E., Benedetti-cecchi, L., Trinanes, J., Muller-karger, F.E., Ambo-rappe, R., Boström,
874 C., Buschmann, A.H., Byrnes, J., Coles, R.G., Creed, J., Cullen-Unsworth, L.C., Diaz-
875 Pulido, G., Duarte, C.M., Edgar, G.J., Fortes, M., Goni, G., Hu, C., Huang, X., Hurd,
876 C.L., Johnson, C., Konar, B., Krause-Jensen, D., Krumhansl, K., Macreadie, P., Marsh,
877 H., McKenzie, L.J., Mieszkowska, N., Miloslavich, P., Montes, E., Nakaoka, M.,
878 Norderhaug, K.M., Norlund, L.M., Orth, R.J., Prathep, A., Putman, N.F., Samper-
879 Villarreal, J., Serrao, E.A., Short, F., Pinto, I.S., Steinberg, P., Stuart-Smith, R.,
880 Unsworth, R.K.F., van Keulen, M., van Tussenbroek, B.I., Wang, M., Waycott, M.,
881 Weatherdon, L. V, Wernberg, T., Yaakub, S.M., 2019. Toward a Coordinated Global
882 Observing System for Seagrasses and Marine Macroalgae. Front. Mar. Sci. 6.
883 https://doi.org/10.3389/fmars.2019.00317
884 Duffy, J.P., Pratt, L., Anderson, K., Land, P.E., Shutler, J.D., 2018. Estuarine, Coastal and
885 Shelf Science Spatial assessment of intertidal seagrass meadows using optical imaging
886 systems and a lightweight drone. Estuar. Coast. Shelf Sci. 200, 169–180.
887 https://doi.org/10.1016/j.ecss.2017.11.001
888 Dutertre, M., Beninger, P.G., Barillé, L., Papin, M., Rosa, P., Barillé, A.-L., Haure, J., 2009.
889 Temperature and seston quantity and quality effects on field reproduction of farmed
890 oysters, *Crassostrea gigas*, in Bourgneuf Bay, France. Aquat. Living Resour. 22, 319–
891 329. https://doi.org/10.1051/alr/2009042
892 Echappé, C., Gernez, P., Méléder, V., Jesus, B., Cognie, B., Decottignies, P., Sabbe, K.,

Barillé, L., 2018. Satellite remote sensing reveals a positive impact of living oyster reefs on microalgal biofilm development. Biogeosciences 15, 905–918. https://doi.org/10.5194/bg-15-905-2018

ESA, 2015. SENTINEL-2 User Handbook. https://doi.org/10.13128/REA-22658

Ferguson, R.L., Korfmacher, K., 1997. Remote sensing and GIS analysis of seagrass meadows in North Carolina, USA. Aquat. Bot. 58, 241–258.

Fyfe, S.K., 2003. Spatial and temporal variation in spectral reflectance: Are seagrass species spectrally distinct? Limnol. Ocean. 48, 464–479.

Gernez, P., Barillé, L., Lerouxel, A., Mazeran, C., Lucas, A., Doxaran, D., 2014. Remote sensing of suspended particulate matter in turbid oyster-farming ecosystems. J. Geophys. Res. Ocean. 119, 7277–7294. https://doi.org/10.1002/2014JC010055

Githaiga, M. N., J. G. Kairo, L. Gilpin, and M. Huxham. 2017. Carbon Storage in the Seagrass Meadows of Gazi Bay, Kenya. PloS One 12(5): e0177001. doi:10.1371/journal. pone.0177001

González-Audícana, M., Otazu, X., Fors, O., Alvarez-Mozos, J., 2006. A low computational-cost method to fuse IKONOS images using the spectral response function of its sensors. IEEE Trans. Geosci. Remote Sens. 44, 1683–1690. https://doi.org/10.1109/TGRS.2005.863299

Hagolle, O., Sylvander, S., Huc, M., Claverie, M., Clesse, D., Dechoz, C., Lonjou, V., Poulain, V., 2015. SPOT-4 (Take 5): simulation of Sentinel-2 time series on 45 large sites. Remote Sens. 7, 12242-12264. https://doi.org/10.3390/rs70912242

Hedley, J.D., Roelfsema, C., Brando, V., Giardino, C., Kutser, T., Phinn, S., Mumby, P.J., Barrilero, O., Laporte, J., Koetz, B., 2018. Coral reef applications of Sentinel-2: Coverage, characteristics, bathymetry and benthic mapping with comparison to Landsat 8. Remote Sens. Environ. 216, 598–614. https://doi.org/10.1016/j.rse.2018.07.014

Hedley, J.D., Roelfsema, C.M., Chollett, I., Harborne, A.R., Heron, S.F., Weeks, S.J., Skirving, W.J., Strong, A.E., Mark Eakin, C., Christensen, T.R.L., Ticzon, V., Bejarano, S., Mumby, P.J., 2016. Remote sensing of coral reefs for monitoring and management: A review. Remote Sens. 8. https://doi.org/10.3390/rs8020118

Hestir, E.L., Brando, V.E., Bresciani, M., Giardino, C., Matta, E., Villa, P., Dekker, A.G., 2015. Measuring freshwater aquatic ecosystems: The need for a hyperspectral global mapping satellite mission. Remote Sens. Environ. 167, 181–195. https://doi.org/10.1016/j.rse.2015.05.023.

Hossain, M.S., Bujang, J.S., Zakaria, M.H., Hashim, M., 2015. The application of remote sensing to seagrass ecosystems: an overview and future research prospects. Int. J. Remote Sens. 36, 61–113. https://doi.org/10.1080/01431161.2014.990649

Huete, A.R., 1988. A Soil-Adjusted Vegetation Index (SAVI). Remote Sens. Environ. 25, 295–309.

Isaksson, T., Kowalski, B., 1993. Piece-Wise Multiplicative Scatter Correction Applied to Near-Infrared Diffuse Transmittance Data from Meat Products. Appl. Spectrosc. 47, 702–709.

Jönsson, P., Eklundh, L., 2004. TIMESAT - A program for analyzing time-series of satellite sensor data. Comput. Geosci. 30, 833–845. https://doi.org/10.1016/j.cageo.2004.05.006

Kaufman, Y.J. and Tanre, D., 1992, Atmospherically resistant vegetation index—ARVI for EOS/MODIS. IEEE Trans. Geosci. Remote Sens., 30, pp. 261– 270.

Kovacs, E., Roelfsema, C., Lyons, M., Zhao, S., Phinn, S., 2018. Seagrass habitat mapping: how do Landsat 8 OLI, Sentinel-2, ZY-3A, and Worldview-3 perform? Remote Sens. Lett. 9, 686–695. https://doi.org/10.1080/2150704X.2018.1468101

Krause-Jensen, D., Lavery, P., Serrano, O., Marbà, N., Masque, P., Duarte, C.M., 2018. Sequestration of macroalgal carbon: the elephant in the Blue Carbon room. Biol. Lett.

14, 1–6. https://doi.org/10.1098/rsbl.2018.0236

Kutser, T., Hedley, H., Giardino, C., Roelfsema, C., Brando, V.E., 2020, Remote sensing of shallow waters – A 50 year retrospective and future directions, Remote Sens. Environ. 240, 111619

Lebreton, B., Richard, P., Radenac, G., Bordes, M., Bréret, M., Arnaud, C., Mornet, F., Blanchard, G.F., 2009. Are epiphytes a significant component of intertidal *Zostera noltii* beds? Aquat. Bot. 91, 82–90.

Lin, H., Sun, T., Zhou, Y., Gu, R., Zhang, X., Yang, W., 2018. Which Genes in a Typical Intertidal Seagrass (*Zostera japonica*) Indicate Pollution? Front. Plant Sci. 9. https://doi.org/10.3389/fpls.2018.01545

Lyons, M.B., Roelfsema, C.M., Phinn, S.R., 2013. Towards understanding temporal and spatial dynamics of seagrass landscapes using time-series remote sensing. Estuar. Coast. Shelf Sci. 120, 42–53. https://doi.org/10.1016/j.ecss.2013.01.015

Lyons, M., Phinn, S., Roelfsema, C., 2011. Integrating Quickbird multi-spectral satellite and field data: Mapping bathymetry, seagrass cover, seagrass species and change in Moreton Bay, Australia in 2004 and 2007. Remote Sens. 3, 42–64. https://doi.org/10.3390/rs3010042

McRoy, C.P., McMillan, C., 1977. Production ecology and physiology of seagrasses. In: McRoy, C.P., Helfferich, C. (Eds.) Seagrass ecosystems: a scientific perspective. Dekker, New York, p 53-81

Milton, E.J., Schaepman, M.E., Anderson, K., Kneubühler, M., Fox, N.P., 2007. Progress in field spectroscopy. Int. Geosci. Remote Sens. Symp. 113, S92–S109. https://doi.org/10.1109/IGARSS.2006.509

Mumby, P.J., Harborne, A.R., 1999. Classification Scheme for Marine Habitats of Belize UNDP/GEF Belize Coastal Zone Management Project Section 1. Introduction and

968 Overview.
969 Nordlund, L.M., Jackson, E.L., Nakaoka, M., Samper-Villarreal, J., Beca-Carretero, P.,
970 Creed, J.C., 2018. Seagrass ecosystem services – What's next? Mar. Pollut. Bull. 134,
971 145–151. https://doi.org/10.1016/j.marpolbul.2017.09.014
972 Nordlund, L.M., Koch, E.W., Barbier, E.B., Creed, J.C., 2016. Seagrass ecosystem services
973 and their variability across genera and geographical regions. PLoS One 11.
974 https://doi.org/10.1371/journal.pone.0163091
975 Orth, R.J., Carruthers, T.J.B., Dennison, W.C., Duarte, C.M., Fourqurean, J.W., Heck, K.L.,
976 Hughes, A.R., Kendrick, G.A., Kenworthy, W.J., Olyarnik, S., Short, F.T., Waycott, M.,
977 Williams, S.L., 2006. A Global Crisis for Seagrass Ecosystems. Bioscience 56, 987–996.
978 https://doi.org/10.1641/0006-3568(2006)56[987:agcfse]2.0.co;2
979 Papathanasopoulou, E., Simis, S., Alikas, K., Ansper, A., Anttila, S., Attila, J., Barillé, A.L,
980 Barillé, L., Brando, V., Bresciani, M., Bučas, M., Gernez, P., Giardino, C., Harin, N.,
981 Hommersom, A., Kangro, K., Kauppila, Koponen, S., Laanen, M., Neil, C., Papadakis,
982 D., Peters, S., Poikane, S., Poser, K., Pires, M.D., Riddick, C., Spyrakos, E., Tyler, A.,
983 Vaičiūtė, D., Warren, M., Zoffoli, M.L., 2019. Satellite-assisted monitoring of water
984 quality to support the implementation of the Water Framework Directive White Paper |
985 November 2019 Satellite-assisted monitoring of water quality to support the
986 implementation of the Water Framework Directive. EOMORES white paper,
987 https://doi.org/10.5281/zenodo.3463051
988 Pendleton, L., Donato, D.C., Murray, B.C., Crooks, S., Jenkins, W.A., Sifleet, S., Craft, C.,
989 Fourqurean, J.W., Kauffman, J.B., Marba, N., Megonigal, P., Pidgeon, E., Herr, D.,
990 Gordon, D., Baldera, A., 2012. Estimating Global 'Blue Carbon' Emissions from
991 Conversion and Degradation of Vegetated Coastal Ecosystems. PLoS One 7.
992 https://doi.org/10.1371/journal.pone.0043542

993 Peralta, G., Brun, F.G., Hernandez, I., Vergara, J.J., Perez-Llorens, J.L., 2005. Morphometric
994 variations as acclimation mechanisms in Zostera noltii beds. Estuar. Coast. Shelf Sci.
995 64, 347–356. https://doi.org/10.1016/j.ecss.2005.02.027
996 Perez-Llorens, J.L., Neill, F.X., 1993. Seasonal dynamics of biomass and nutrient content in
997 the intertidal seagrass Zostera noltii Hornem from Palmones River estuary, Spain.
998 Aquat. Bot. 46, 49–66.
999 Pettorelli, N., Vik, J.O., Mysterud, A., Gaillard, J.M., Tucker, C.J., Stenseth, N.C., 2005.
1000 Using the satellite-derived NDVI to assess ecological responses to environmental
1001 change. Trends Ecol. Evol. 20, 503–510. https://doi.org/10.1016/j.tree.2005.05.011
1002 Philippart, C.J.M., Dijkema, K.S., 1995. Wax and wane of *Zostera noltii* in the Dutch
1003 Wadden Sea. Aquat. Bot. 49, 255–268. https://doi.org/10.1016/0304-3770(94)00431-K
1004 Phinn, S.R., Kovacs, E.M., Roelfsema, C.M., Canto, R.F., Collier, C.J., McKenzie, L.J.,
1005 2018a. Assessing the potential for satellite image monitoring of seagrass thermal
1006 dynamics: for inter- and shallow sub-tidal seagrasses in the inshore Great Barrier Reef
1007 World Heritage Area, Australia. Int. J. Digit. Earth 11, 803–824.
1008 https://doi.org/10.1080/17538947.2017.1359343
1009 Phinn, S., Roelfsema, C., Kovacs, E., Canto, R., Lyons, M., Saunders, M., & Maxwell, P.,
1010 2018b. Mapping, monitoring and modelling seagrass using remote sensing techniques.
1011 In: Larkum, A., Kendrick, G., Ralph, P. (Eds.). Seagrasses of Australia (pp. 445-487).
1012 Springer, Cham.
1013 Phinn, S., Roelfsema, C., Dekker, A., Brando, V., Anstee, J., 2008. Mapping seagrass species,
1014 cover and biomass in shallow waters: An assessment of satellite multi-spectral and
1015 airborne hyper-spectral imaging systems in Moreton Bay (Australia). Remote Sens.
1016 Environ. https://doi.org/10.1016/j.rse.2007.09.017

1017 Postlethwaite, V.R., McGowan, A.E., Kohfeld, K.E., Robinson, C.L.K., Pellatt, M.G., 2018.
1018 Low blue carbon storage in eelgrass (*Zostera marina*) meadows on the Pacific Coast of
1019 Canada. PLoS One 13. https://doi.org/10.1371/journal.pone.0198348
1020 Prabhakara, K., Dean Hively, W., McCarty, G.W., 2015. Evaluating the relationship between
1021 biomass, percent groundcover and remote sensing indices across six winter cover crop
1022 fields in Maryland, United States. Int. J. Appl. Earth Obs. Geoinf. 39, 88–102.
1023 https://doi.org/10.1016/j.jag.2015.03.002
1024 Roelfsema, C.M., Lyons, M., Kovacs, E.M., Maxwell, P., Saunders, M.I., Samper-Villarreal,
1025 J., Phinn, S.R., 2014. Multi-temporal mapping of seagrass cover, species and biomass: A
1026 semi-automated object based image analysis approach. Remote Sens. Environ. 150, 172–
1027 187. https://doi.org/10.1016/j.rse.2014.05.001
1028 Roelfsema, C., Kovacs, E.M., Saunders, M.I., Phinn, S., Lyons, M., Maxwell, P., 2013.
1029 Challenges of remote sensing for quantifying changes in large complex seagrass
1030 environments. Estuar. Coast. Shelf Sci. 133, 161–171.
1031 https://doi.org/10.1016/j.ecss.2013.08.026
1032 Roy, D.P., Li, J., Zhang, H.K., Yan, L., Huang, H., Li, Z., 2017. Examination of Sentinel-2A
1033 multi-spectral instrument (MSI) reflectance anisotropy and the suitability of a general
1034 method to normalize MSI reflectance to nadir BRDF adjusted reflectance. Remote Sens.
1035 Environ. 199, 25–38. https://doi.org/10.1016/j.rse.2017.06.019
1036 Saderne, V., Geraldi, N.R., Macreadie, P.I., Maher, D.T., Middelburg, J.J., Serrano, O.,
1037 Almahasheer, H., Arias-Ortiz, A., Cusack, M., Eyre, B.D., Fourqurean, J.W., Kennedy,
1038 H., Krause-Jensen, D., Kuwae, T., Lavery, P.S., Lovelock, C.E., Marba, N., Masqué, P.,
1039 Mateo, M.A., Mazarrasa, I., McGlathery, K.J., Oreska, M.P.J., Sanders, C.J., Santos,
1040 I.R., Smoak, J.M., Tanaya, T., Watanabe, K., Duarte, C.M., 2019. Role of carbonate
1041 burial in Blue Carbon budgets. Nat. Commun. https://doi.org/10.1038/s41467-019-

1042 08842-6
1043 Sani, D.A., Hashim, M., Hossain, M.S., 2019. Recent advancement on estimation of blue
1044 carbon biomass using satellite-based approach. Int. J. Remote Sens. 1–37.
1045 https://doi.org/10.1080/01431161.2019.1601289
1046 Short, F., Carruthers, T., Dennison, W., Waycott, M., 2007. Global seagrass distribution and
1047 diversity: A bioregional model. J. Exp. Mar. Bio. Ecol. 350, 3–20.
1048 https://doi.org/10.1016/j.jembe.2007.06.012
1049 Sims, D.A., Gamon, J.A., 2002. Relationships between leaf pigment content and spectral
1050 reflectance across a wide range of species, leaf structures and developmental stages.
1051 Remote. Sens. Environ. 81, 337–354.
1052 Soissons, L.M., Haanstra, E.P., van Katwijk, M.M., Asmus, R., Auby, I., Barillé, L., Brun,
1053 F.G., Cardoso, P.G., Desroy, N., Fournier, J., Ganthy, F., Garmendia, J.-M., Godet, L.,
1054 Grilo, T.F., Kadel, P., Ondiviela, B., Peralta, G., Puente, A., Recio, M., Rigouin, L.,
1055 Valle, M., Herman, P.M.J., Bouma, T.J., 2018. Latitudinal Patterns in European Seagrass
1056 Carbon Reserves: Influence of Seasonal Fluctuations versus Short-Term Stress and
1057 Disturbance Events. Front. Plant Sci. 9, 1–12. https://doi.org/10.3389/fpls.2018.00088
1058 Thome, K.J., Biggar, S.F., Wisniewski, W., 2003. Cross comparison of EO-1 sensors and
1059 other earth resources sensors to Landsat-7 ETM+ using Railroad Valley Playa. IEEE
1060 Trans. Geosci. Remote Sens. 41, 1180–1188.
1061 https://doi.org/10.1109/TGRS.2003.813210
1062 Traganos, D., Aggarwal, B., Poursanidis, D., Topouzelis, K., Chrysoulakis, N., Reinartz, P.,
1063 2018. Towards global-scale seagrass mapping and monitoring using Sentinel-2 on
1064 Google Earth Engine: The case study of the Aegean and Ionian Seas. Remote Sens. 10,
1065 1–14. https://doi.org/10.3390/rs10081227
1066 Traganos, D., Reinartz, P., 2018. Interannual Change Detection of Mediterranean Seagrasses

1067 Using RapidEye Image Time Series. Front. Plant Sci. 9.
1068 https://doi.org/10.3389/fpls.2018.00096
1069 Tucker, C.J., 1979. Red and photographic infrared linear combinations for monitoring
1070 vegetation. Remote Sens. Environ. 8, 127–150. https://doi.org/10.1016/0034-
1071 4257(79)90013-0
1072 Unsworth, R.K.F., Mckenzie, L.J., Collier, C.J., Cullen-Unsworth, L.C., Duarte, C.M., Eklof,
1073 J.S., Jarvis, J.C., Jones, B.L., Nordlund, L.M., 2019. Global challenges for seagrass
1074 conservation. Ambio 48, 801–815. https://doi.org/10.1007/s13280-018-1115-y
1075 Unsworth, R.K.F., Nordlund, L.M., Cullen-Unsworth, L.C., 2018. Seagrass meadows support
1076 global fisheries production. Conserv. Lett. 1–8. https://doi.org/10.1111/conl.12566
1077 USGS, 2018. LANDSAT 8 (L8) DATA USERS HANDBOOK. Version 3.0. Sioux Falls,
1078 South Dakota.
1079 Valle, M., Chust, G., del Campo, A., Wisz, M.S., Olsen, S.M., Garmendia, J.M., Borja, Á.,
1080 2014. Projecting future distribution of the seagrass Zostera noltii under global warming
1081 and sea level rise. Biol. Conserv. 170, 74–85.
1082 https://doi.org/10.1016/j.biocon.2013.12.017
1083 Valle, M., Palà, V., Lafon, V., Dehouck, A., Garmendia, J.M., Borja, Á., Chust, G., 2015.
1084 Mapping estuarine habitats using airborne hyperspectral imagery, with special focus on
1085 seagrass meadows. Estuar. Coast. Shelf Sci. 164, 433–442.
1086 https://doi.org/10.1016/j.ecss.2015.07.034
1087 van der Wal, D., Wielemaker-van den Dool, A., Herman, P.M.J., 2010. Spatial synchrony in
1088 intertidal benthic algal biomass in temperate coastal and estuarine ecosystems.
1089 Ecosystems 13, 338–351. https://doi.org/10.1007/s10021-010-9322-9
1090 Vanhellemont, Q., 2009. Use of MODIS imagery for the assessment of the variability in
1091 intertidal microphytobenthos biomass at regional and global scales. Thesis. Universiteit

Gent.

Vermaat, J.E., Verhagen, F.C.A., 1996. Seasonal variation in the intertidal seagrass Zostera noltii Hornem.: Copuling demographic and physiological patterns. Aquat. Bot. 52, 259–281. https://doi.org/10.1016/0304-3770(95)00510-2

Vermote, E., Justice, C.O., Bréon, F.M., 2009. Towards a generalized approach for correction of the BRDF effect in MODIS directional reflectances. IEEE Trans. Geosci. Remote Sens. 47, 898–908. https://doi.org/10.1109/TGRS.2008.2005977

Villa, P., Laini, A., Bresciani, M., Bolpagni, R., 2013. A remote sensing approach to monitor the conservation status of lacustrine Phragmites australis beds. Wetl. Ecol. Manag. 21, 399–416. https://doi.org/10.1007/s11273-013-9311-9

Villa, P., Mousivand, A., Bresciani, M., 2014. Aquatic vegetation indices assessment through radiative transfer modeling and linear mixture simulation. Int. J. Appl. Earth Obs. Geoinf. 30, 113–127. https://doi.org/10.1016/j.jag.2014.01.017

Wang, D., Wan, B., Qiu, P., Su, Y., Guo, Q., Wang, R., Sun, F., Wu, X., 2018. Evaluating the performance of Sentinel-2, Landsat 8 and Pléiades-1 in mapping mangrove extent and species. Remote Sens. 10. https://doi.org/10.3390/rs10091468

Ward, D.H., Morton, A., Tibbitts, T.L., Douglas, D.C., Carrera-González, E., 2003. Long-term Change in Eelgrass Distribution at Bahía San Quintín, Baja California, Mexico, using Satellite Imagery. Estuaries 26, 1529–1539. https://doi.org/10.1007/BF02803661

Ward, D.H., Markonb, C.J., Douglas, D.C., 1997. Distribution and stability of eelgrass beds at Izembek Lagoon, Alaska. Aquat. Bot. 58, 229–240.

Waycott, M., Duarte, C.M., Carruthers, T.J.B., Orth, R.J., Dennison, W.C., Olyarnik, S., Calladine, A., Fourqurean, J.W., Heck, K.L., Hughes, A.R., Kendrick, G.A., Kenworthy, W.J., Short, F.T., Williams, S.L., 2009. Accelerating loss of seagrasses across the globe threatens coastal ecosystems. Proc. Natl. Acad. Sci. 106, 12377–12381.

https://doi.org/10.1073/pnas.0905620106

Waycott, M., Longstaff, B.J., Mellors, J., 2005. Seagrass population dynamics and water quality in the Great Barrier Reef region: A review and future research directions. Mar. Pollut. Bull. 51, 343–350. https://doi.org/10.1016/j.marpolbul.2005.01.017

Zoffoli, M.L., Kandus, P., Madanes, N., Calvo, D.H., 2008. Seasonal and interannual analysis of wetlands in South America using NOAA-AVHRR NDVI time series: The case of the Parana Delta Region. Landsc. Ecol. 23. https://doi.org/10.1007/s10980-008-9240-9

Acknowledgments

We acknowledge the students of the "Ecosystem and Marine Bioproduction" and "Aquaculture, Environment and Society" Master programs of Nantes University (2018/2019 and 2019/2020) for their participation in field data acquisition. The European Space Agency is acknowledged for the provision of Sentinel-2 and Worldview-2 images, and for the distribution of the SNAP software. We thank the Laboratory of Planetology and Geodynamics (LPG) of Nantes University for the use of the ASD spectroradiometer. We also thank the anonymous reviewers for their valuable contributions to improve our manuscript. We especially thank Dr. Stephanie Palmer for revising the English of the manuscript.

Author contributions: MLZ: conceptualization, field work, data processing and analysis, investigation, methodology, writing–original draft. PG and LB: conceptualization, field work, data analysis, investigation, methodology, writing–original draft, funding acquisition, project administration. VB: data analysis, writing–original draft, funding acquisition. PR, ALB, ALB, NH: field work, data processing, writing–original draft. SP, KP: funding acquisition, writing–original draft. LS: data processing, writing–original draft. GP: field work, writing–original draft.

Funding: This project has received funding from the European Union's Horizon 2020 research and innovation programme (Grant agreement n° 776348 - CoastObs).

Appendix

As the radiometric measurements were taken within a time interval of approximately four hours (± 2 hours from low tide), the illumination angle naturally changed between the radiometric acquisitions. The multiplicative scatter correction (MSC; Isaksson and Kowalski, 1993, Fyfe, 2003) technique consists of applying a multiplicative factor and an offset to each sampled reflectance spectrum. These factors were obtained from linear least-squares regressions between every single spectrum and a reference. A key step in this technique is the choice of the reference. As in our case the measurements were not performed over the same target, a single reference could not be used for all spectra, and different references were computed according to the range of seagrass percent cover. For each area and year sampled, we simulated a series of 11 reflectance references for hypothetical seagrass percent cover, varying from 0 to 100% at 10% intervals. First, the 0% and 100% references were obtained from the average of > 3 measurements over the pure substrates, corresponding to bare sediment and full seagrass cover respectively. Then, the intermediate reference spectra were computed through a linear combination of the references of these two pure substrates. Second, the reflectance dataset was clustered into 11 classes by seagrass cover (0-5%, 5-15%, ..., 85-95%, 95-100%), and the corresponding reference spectrum was used to apply the MSC correction to all *in situ* spectra within each cluster. The radiometric MSC correction applied to *in situ* spectra clearly improved the quality of the data (Figure A1a, b). Also note that, even though this correction was applied independently to each dataset, it improves the significance of ANCOVA tests performed between datasets collected in Bourgneuf Bay in 2018 and 2019. The shape and amplitude of the corrected spectra exhibited variations consistent with the progressive increase in seagrass cover. Also, the goodness-of-fit was improved by applying the MSC correction, showing better adjustment with SPC_{cores} (Figure A1c, d).

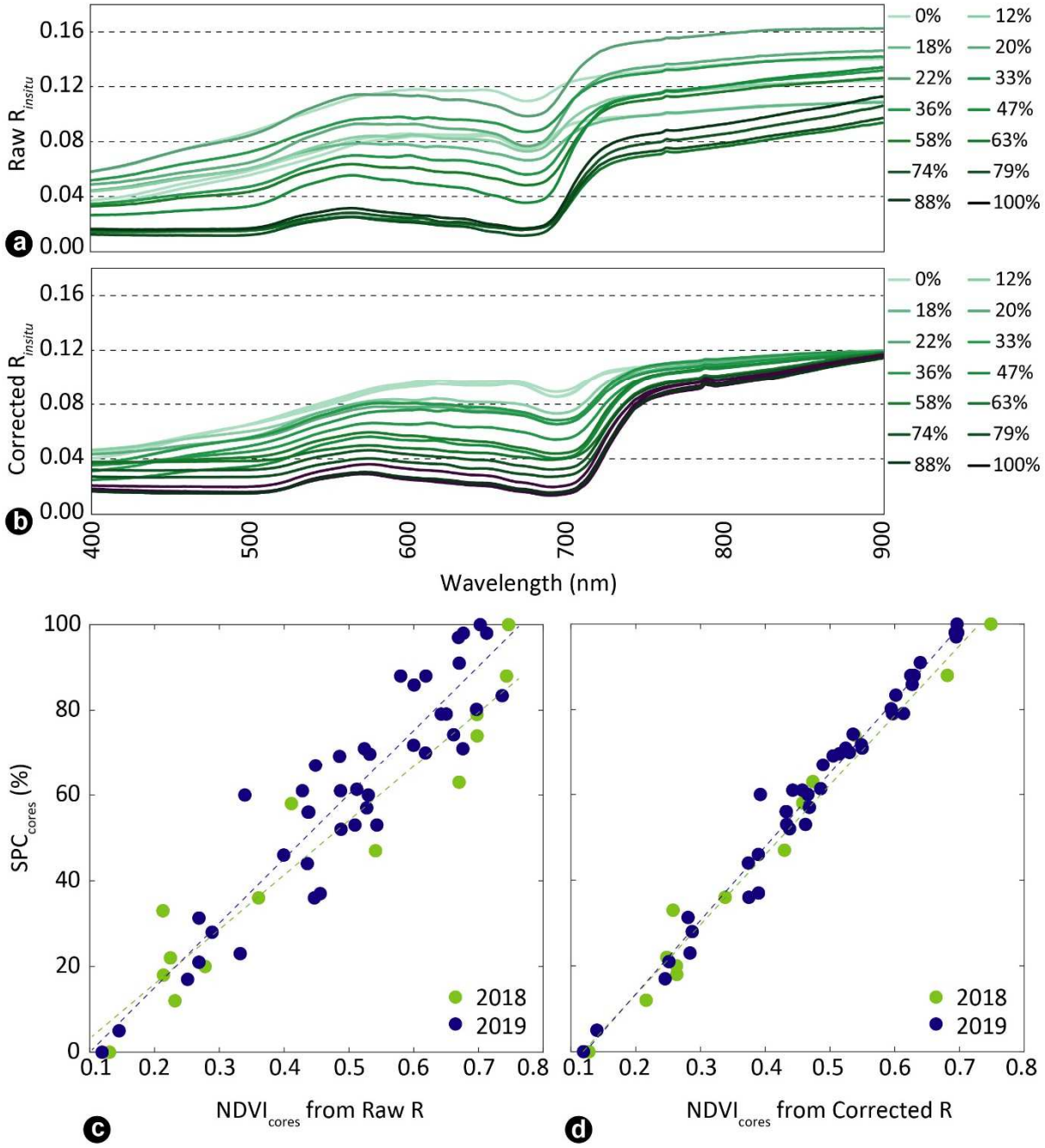

Figure A1: (a) Raw reflectance spectra as a function of wavelength obtained from Equation 1. (b) Reflectance spectra corrected following the MSC technique. In panels (a) and (b), the same intensity gradient was used, with darker colors representing higher percentages of seagrass cover. (c-d) Seagrass percent cover measured *in situ* (SPC_{cores}) in Bourgneuf Bay as a function of $NDVI_{cores}$. Green dots refer to data collected in 2018 and blue dots to data from 2019. Panel (c) presents $NDVI_{cores}$ data derived from R_{insitu} spectra before MSC correction, while panel (d) shows R_{insitu} spectra following the application of MSC correction.

Table A1. Multispectral vegetation indices (VIs) tested in this study to describe seagrass percent cover (SPC_{cores}) with their corresponding equations. For each spectral index that did not show significant differences between 2018 and 2019 (i.e., ANCOVA $p > 0.05$), the coefficient of determination (R^2) (with $p < 0.01$ for all linear regressions) and RMSD between the *in situ* percent cover and the VI are provided. The following VIs were compared: normalized difference vegetation index (NDVI), normalized difference aquatic vegetation index (NDAVI), water adjusted vegetation index (WAVI), soil-adjusted vegetation index (SAVI), atmospherically resistant vegetation index (ARVI), modified narrow-band NDVI (mNDVI), and modified normalized difference (mND).

		MSC corrected spectra		
Index	**Equation**	**ANCOVA (p)**	**R^2**	**RMSD**
NDVI(665,842)	$\frac{R(842) - R(665)}{R(842) + R(665)}$	**0.243**	**0.978**	4.14
NDVI(705,842)	$\frac{R(842) - R(705)}{R(842) + R(705)}$	**0.964**	**0.955**	5.88
NDAVI(490,842)	$\frac{R(842) - R(490)}{R(842) + R(490)}$	**0.492**	**0.977**	4.19
WAVI(490,842)	$(1 + 0.5)\frac{R(842) - R(490)}{R(842) + R(490) + 0.5}$	$1.03e^{-08}$	Not evaluated	Not evaluated
SAVI(665,842)	$(1 + 0.5)\frac{R(842) - R(665)}{R(842) + R(665) + 0.5}$	0.000	Not evaluated	Not evaluated
ARVI(490,665,842)	$\frac{R(842) - R(665) - (R(490) - R(665))}{R(842) + R(665) - (R(490) - R(665))}$	**0.107**	**0.956**	5.82
mNDVI(490,665,842)	$\frac{R(842) - R(665)}{R(842) + R(665) - 2R(490)}$	**0.194**	**0.820**	11.7
mNDVI(443,665,740)	$\frac{R(740) - R(665)}{R(740) + R(665) - 2R(443)}$	**0.055**	**0.853**	10.6
mND(443,705,740)	$\frac{R(740) - R(705)}{R(740) + R(705) - 2R(443)}$	**0.921**	**0.851**	10.7

Table A2. Date and time of S2 image acquisitions during low tide and cloud-free conditions used in this work. Satellite information (S2A/B), orbit number, tidal height (m), and tidal stage at the time of image acquisition, phase of seagrass seasonal cycle, and usage of the scene for this work are also provided. Dates coincident with fieldwork are highlighted in bold.

Date	Time (GMT)	Satellite	Orbit Number	Tidal height (m)	Tidal stage	Phase of Seagrass seasonal cycle	Scene used for
30/03/2018	10:56:19	S2B	094	1.84	Spring tide	Latency phase	Seasonal cycle
17/04/2018	11:06:51	S2A	137	0.64	Spring tide	Latency phase	Seasonal cycle, Evaluation of impacts of seasonal variability on SPC
19/04/2018	10:56:19	S2B	094	1.46	Spring tide	Latency phase	Seasonal cycle
04/05/2018	10:56:21	S2A	094	2.50	Spring tide	Latency phase	Seasonal cycle
19/05/2018	10:56:19	S2B	094	2.23	Spring tide	Increasing phase	Seasonal cycle
13/06/2018	10:56:21	S2A	094	2.01	Spring tide	Increasing phase	Seasonal cycle
26/06/2018	11:06:21	S2A	137	2.95	Neap tide	Increasing phase	Seasonal cycle
28/06/2018	10:56:19	S2B	094	1.61	Spring tide	Increasing phase	Seasonal cycle
01/07/2018	11:06:19	S2B	137	1.81	Spring tide	Increasing phase	Seasonal cycle
13/07/2018	10:56:21	S2A	094	1.24	Spring tide	Increasing phase	Seasonal cycle, Evaluation of impacts of seasonal variability on SPC
16/07/2018	11:06:21	S2A	137	1.32	Spring tide	Increasing phase	Seasonal cycle
02/08/2018	10:56:21	S2A	094	2.99	Neap tide	Increasing phase	Seasonal cycle
01/09/2018	10:56:21	S2A	094	3.19	Spring tide	Peak	Selection of pixels to reconstruct seasonal cycle, Seasonal cycle
09/09/2018	11:06:09	S2B	137	2.01	Spring tide	Peak	Seasonal cycle
14/09/2018	11:06:51	S2A	137	1.08	Spring tide	Peak	Seasonal cycle, SPC and SB maps, Evaluation of impacts of seasonal variability on SPC
24/09/2018	11:08:01	S2A	137	2.17	Spring tide	Peak	Seasonal cycle
26/09/2018	11:00:29	S2B	094	1.08	Spring tide	Peak	Atmospheric correction evaluation, Seasonal cycle. Comparison with WV02 map
27/09/2018	11:22:32	WV02		0.96	Spring tide	Peak	Evaluation of S2 spatial resolution
29/09/2018	11:08:29	S2B	137	1.79	Spring tide	Decreasing phase	Seasonal cycle, Evaluation of impacts of seasonal variability

							on SPC
09/10/2018	11:09:39	S2B	137	1.43	Spring tide	Decreasing phase	Seasonal cycle
08/11/2018	11:12:49	S2B	137	1.29	Spring tide	Decreasing phase	Seasonal cycle
13/11/2018	11:13:11	S2A	137	3.16	Neap tide	Decreasing phase	Seasonal cycle
10/12/2018	11:04:31	S2A	094	1.59	Spring tide	Latency phase	Seasonal cycle, Evaluation of impacts of seasonal variability on SPC
23/03/2019	11:07:21	S2A	137	0.32	Spring tide	Latency phase	Seasonal cycle
09/04/2019	10:56:21	S2A	094	1.71	Spring tide	Latency phase	Seasonal cycle
19/04/2019	10:56:21	S2A	094	1.00	Spring tide	Latency phase	Seasonal cycle
19/05/2019	10:56:21	S2A	094	0.99	Spring tide	Latency phase	Seasonal cycle
06/06/2019	11:06:29	S2B	137	1.12	Spring tide	Increasing phase	Seasonal cycle
16/06/2019	11:06:29	S2B	137	2.50	Spring tide	Increasing phase	Seasonal cycle
18/06/2019	10:56:21	S2A	094	1.17	Spring tide	Increasing phase	Seasonal cycle
21/06/2019	11:06:21	S2A	137	2.00	Spring tide	Increasing phase	Seasonal cycle
03/07/2019	10:56:29	S2B	094	1.35	Spring tide	Increasing phase	Seasonal cycle
06/07/2019	11:06:29	S2B	137	1.41	Spring tide	Increasing phase	Seasonal cycle
16/07/2019	11:06:29	S2B	137	2.10	Spring tide	Increasing phase	Seasonal cycle
21/07/2019	11:06:31	S2A	137	2.11	Spring tide	Increasing phase	Seasonal cycle
31/07/2019	11:06:21	S2A	137	2.58	Spring tide	Increasing phase	Seasonal cycle
02/08/2019	10:56:29	S2B	094	0.61	Spring tide	Increasing phase	Seasonal cycle
20/08/2019	11:06:21	S2A	137	2.10	Spring tide	Peak	Seasonal cycle
01/09/2019	10:56:19	S2B	094	0.24	Spring tide	Peak	Atmospheric correction evaluation, Seasonal cycle
11/09/2019	10:56:29	S2B	094	3.25	Neap tide	Peak	Evaluation of impacts of tide height on SPC
16/09/2019	10:57:01	S2A	094	1.16	Spring tide	Peak	Seasonal cycle
19/09/2019	11:07:21	S2A	137	2.16	Spring tide	Peak	Seasonal cycle
29/09/2019	11:08:41	S2A	137	0.99	Spring tide	Decreasing phase	Seasonal cycle

1195

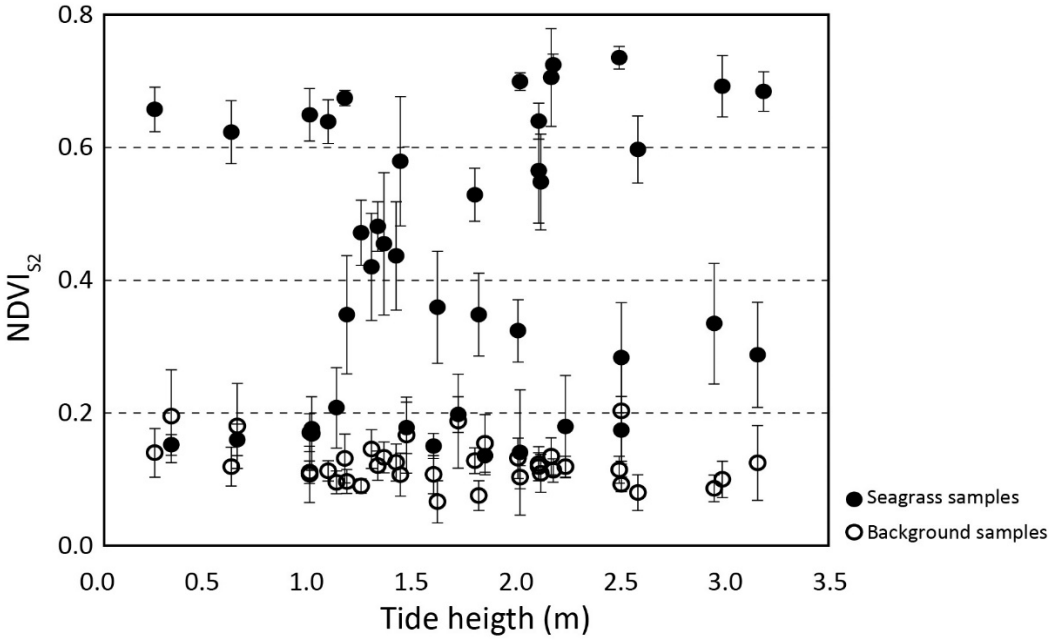

1196

1197 **Figure A2:** Median $NDVI_{S2}$ of seagrass samples (dimensionless, in solid dots) used to

1198 reconstruct the seasonal cycle as a function of tidal height (m). Open dots correspond to

1199 background samples. Error bars represent the IQR.

1200

1201

Figure captions

Figure 1. Study area. (a) Locations of study sites along the northeastern Atlantic coast. (b-c) Field view of the Bourgneuf Bay seagrass meadow in September, 2018. (d) Close-up of high percent cover of *Zostera noltei* in Bourgneuf Bay in 2018. (e) Quasi true-color composition (R: 660 nm, G: 545 nm, B: 480 nm) of the Worldview2 image acquired on September 27, 2018 for Bourgneuf Bay, showing the seagrass meadow, macroalgae, and aquaculture areas.

Figure 2. Flowchart of the main methodological steps used in the present study to compute: (a) seagrass percent cover (SPC) and (b) seagrass leaf biomass (SB) from S2 data.

Figure 3. (a) Selected photos of seagrass cover before core sampling, illustrating the differences between 0 and 100% cover. (b-c) Relationship between the S2-simulated *in situ* NDVI ($NDVI_{cores}$) and seagrass biological descriptors obtained from the 2018 (green dots) and 2019 (blue) core data from Bourgneuf Bay. Panels (b) and (c) represent $NDVI_{cores}$ as a function of seagrass percent cover (SPC_{cores}) and seagrass leaf biomass (SB_{cores}; g DW m^{-2}) respectively, encompassing the entire dataset (including both developing and evaluation subsets).

Figure 4. Linear models used for algorithm development: (a) SPC_{cores} *vs.* $NDVI_{cores}$ and (b) SB_{cores} *vs.* $NDVI_{cores}$.

Figure 5. Validation of S2 atmospheric correction over the Bourgneuf Bay emerged seagrass meadow. (a) Comparison between *in situ* (R_{insitu}; solid line with circles) and satellite ($R_{sat\text{-}S2}$; dashed lines with squares) reflectance spectra in 2018, for three types of target: bare sediment, mixed area, and dense seagrass cover in orange, black, and green lines respectively. (b) Same as in (a) but for 2019, and for only two types of target: bare sediment and dense seagrass cover. (c) Match-ups between $R_{sat\text{-}WV02}$ and R_{insitu} in 2018 and 2019, using all S2 spectral bands from 443 – 865 nm.

Figure 6. Same as in Figure 5, but for the validation of WV02 atmospheric correction on the September 27, 2018.

Figure 7. $NDVI_{S2}$ seasonal cycle in Bourgneuf Bay intertidal seagrass beds in 2018 and 2019, from March to December. Red and blue symbols correspond to the NDVI of the seagrass pixels (median ± IQR), with the dashed line corresponding to a Gaussian model fit. In Bourgneuf Bay there is overlap of two S2 orbital cycles, with orbits #137 and #94 in blue and red respectively. Black symbols correspond to the background pixels extracted over bare sediment (median ± IQR). No distinction between the two orbits was done for the background

pixels. The green arrows correspond to the dates of images selected to best represent maximum annual growth and used for mapping.

Figure 8. Validation of S2-derived seagrass percent cover (SPC_{S2}) *vs. in situ* measurements (SPC_{insitu}) acquired in 2018 (green dots) and 2019 (blue dots). The dashed line shows the linear regression between SPC_{S2} and SPC_{insitu}, whereas the continuous line shows the 1:1 relationship.

Figure 9. Sentinel-2 maps of (a-b) NDVI, (c-d) seagrass percent cover (SPC), and (d-e) leaf seagrass biomass (SB), during summer maximum in Bourgneuf Bay (2018 for panels on the left side and 2019, on the right). The grayscale background corresponds to areas of seagrass beds. The black lines show the 0 – 3 m (LAT) isobaths.

Figure 10. (a) Close-up of the seagrass percent cover map during the *Z. noltei* annual peak in 2018 based on Sentinel-2 data, with white arrows pointing to intertidal channels. (b) Location of the close-up panel within the seagrass meadow. The black lines show the 0 – 3 m (LAT) isobaths.

Figure 11. Demonstration of seasonal changes in seagrass percent spatial distribution using S2 images of different seasonal cycle stages in 2018: (a) latency phase on April 17, (b) increasing phase on July 13, (c) annual peak on September 14, (d) decreasing phase on September 29, and (e) latency phase on December 10. Panels (f-j) are close-ups of the area indicated in panels (a-e) within the seagrass meadow.

Figure 12. (a) Comparison of $NDVI_{WV02\text{-}recalibrated}$ obtained on September 27, 2018 with $NDVI_{S2}$ obtained on September 26, 2018. (b) Effective total surface occupied by seagrass (in km^2) derived from S2 (in black bars) and WV02 (in gray bars) for different classes of SPC ≥ 20%.

Figure 13. SPC maps at different pixel sizes, using (a) S2 data (10 m) from September 26, 2018 and (b) WV02 data (2 m) from September 27, 2018. Panels (c-f) show two close-up areas in within the seagrass beds, indicated in panels (a) and (b).

Figure 14. Demonstration of the effect of tidal differences on $NDVI_{S2}$ spatial distribution on (a) September 1, 2019 and (b) September 11, 2019. (c) The $NDVI_{S2}$ obtained along one transect (indicated in the maps of panels (a) and (b)) from September 1, 2019 (green line) and September 11, 2019 (in orange). Black arrows indicate the waterfront that corresponds to the boundary between emersed and immersed areas at the time of image acquisition on both

dates. The blue area shows the difference in the waterfront distance (in image pixels) along the transect between the two dates.

Table captions

Table 1. Summary of fieldwork campaigns, including dates and sample size per parameter.

Table 2. Uncertainty metrics (R^2, slope, RMSD, Bias, MAD, and sample size (N) used to validate seagrass algorithms with datasets from the three regions.

Table 3. S2/MSI NDVI adjustment for other multispectral sensors. For each sensor, the gain (m) and offset (b) has to be used in a linear equation: NDVI/S2 = m NDVI/sensor + b.

Table 4. NDVI ranges for sparse/dense seagrass cover classes for several multispectral sensors.